Vertical Momentum Transports Associated with Moist Convection and Gravity Waves in a Minimal Model of QBO-like Oscillation

ERIKO NISHIMOTO AND SHIGEO YODEN

Department of Geophysics, Kyoto University, Kyoto, Japan

HOANG-HAI BUI

Hanoi University of Science, Vietnam National University, Hanoi, Vietnam

(Manuscript received 4 September 2015, in final form 4 April 2016)

ABSTRACT

A self-sustained oscillation dynamically analogous to the equatorial quasi-biennial oscillation (QBO) was obtained as a radiative–moist-convective quasi-equilibrium state in a minimal model of the stratosphere–troposphere coupled system, which is a two-dimensional cloud-system-resolving nonhydrostatic model with a periodic lateral boundary condition. The QBO-like oscillation shows downward propagation of the zonal mean signals in the stratosphere. In addition, in the troposphere there are periodic variations associated with the QBO-like oscillation, including organized features of moist-convective systems characterized as squall-line- or back-building-type precipitation patterns. Details of the momentum budget variation are examined to study the stratosphere–troposphere dynamical coupling associated with the QBO-like oscillation. The vertical flux of horizontal momentum is separated into three contributions of convective momentum transport (CMT) and momentum transports by upward- and downward-propagating gravity waves—that is, upward and downward gravity wave momentum transports (GWMTs)—and the time–height variations of each contribution are evaluated quantitatively. The method is based on the linear theory of gravity waves to separate upward- and non-upward-propagating contributions and uses the phase speed spectra of the total cloud mixing ratio to identify the CMT contribution. The upward GWMT predominates in the stratosphere and contributes to the acceleration of the zonal mean zonal wind. The CMT and downward GWMT are confined to the troposphere, and the former predominates. The variations of the mean zonal wind modulate the organization of convective systems, and the squall-line- and back-building-type patterns appear alternately. According to the modulation of convective systems, the spectral features of every momentum transport vary periodically.

1. Introduction

The quasi-biennial oscillation (QBO) is observed as the dominant variation of the equatorial stratosphere (~16–50 km) and characterized as downward-propagating easterly and westerly mean zonal wind, with periods averaging approximately 28 months (e.g., Baldwin et al. 2001). The QBO is considered to be an internal oscillation due to wave–mean flow interactions under the zonally periodic boundary condition; in the oscillation, waves are generated in the troposphere and propagate into the stratosphere. Theoretical works on the QBO assumed the separation of the troposphere from the stratosphere to focus on the interactions in the stratosphere (e.g., Lindzen and Holton 1968; Holton and Lindzen 1972). However, there is not such a clear separating boundary between the stratosphere and the troposphere.

Held et al. (1993) introduced a two-dimensional cloud-system-resolving regional model with explicit stratosphere and troposphere under a periodic lateral boundary condition, and they obtained a QBO-like oscillation in a radiative–moist-convective quasi-equilibrium state. It is a self-sustained oscillation in the minimal model of the QBO in a stratosphere–troposphere coupled system without effects of the rotation of the earth nor the zonal mean upwelling of the Brewer–Dobson circulation. We reexamined the QBO-like oscillations in such an idealized dynamical framework with a state-of-the-art regional cloud-system-resolving model and showed the robustness

Corresponding author address: Eriko Nishimoto, Department of Geophysics, Kyoto University, Kitashirakawa Oiwake-cho, Sakyo-ku, Kyoto 606-8502, Japan.
E-mail: eriko@kugi.kyoto-u.ac.jp

DOI: 10.1175/JAS-D-15-0265.1

of the oscillation insensitive to the choice of model configuration and parameters (Yoden et al. 2014, hereafter YBN14). The obtained QBO-like oscillations show downward propagation of the zonal mean signals in the stratosphere and associated periodic variations in the troposphere. Such tropospheric variations associated with the QBO-like oscillations may be weakened or smeared by the influences of complicated processes in the real atmosphere that are not included in the minimal model. However, such a model can be a test bed to study possible dynamical processes of the stratosphere–troposphere coupling associated with the QBO.

Takahashi (1993) also obtained a QBO-like oscillation and associated variations in the troposphere in a two-dimensional model of stratosphere–troposphere coupled system along the equator that was derived from a general circulation model (GCM). His simplified model had very coarse resolutions and employed a convective parameterization without the rotation of the earth. Horinouchi and Yoden (1998) conducted aquaplanet numerical experiments with a three-dimensional GCM and obtained QBO-like oscillations in the stratosphere and signals of associated variations in the troposphere. However, these studies mainly analyzed the stratospheric part of the oscillation, whereas the associated variations in the troposphere had received little attention. Downward influence of the QBO-like oscillations on the troposphere has not been studied yet.

The use of a hierarchy of numerical models is needed to reduce the gap between an idealized theory and the complex real atmosphere (Hoskins 1983; Held 2005). As stated in YBN14, it would be a good timing to reinvestigate the dynamics of the QBO-like oscillations obtained in the hierarchy of idealized regional and global models in two and three dimensions from a viewpoint of stratosphere–troposphere dynamical coupling in the tropics.

In this study, we examine the momentum budget of a self-sustained oscillation dynamically analogous to the equatorial QBO that was obtained by YBN14 in a stratosphere–troposphere coupled system. It will be shown that organized features of moist-convective systems vary rather periodically associated with the QBO-like oscillation. Two processes are associated with the vertical momentum transport in this two-dimensional experiment with a cloud-system-resolving model. One is convective momentum transport (CMT), which occurs primarily in the troposphere and is due to organized circulations associated with slantwise convections (e.g., Moncrieff 1992). The other is gravity wave momentum transport (GWMT), which is associated with vertically propagating gravity waves generated by convection (e.g., Fritts and Alexander 2003).

Regional cloud-system-resolving models in two dimensions have been used to investigate stratospheric gravity waves generated by a squall-line type of convection (Fovell et al. 1992; Alexander et al. 1995) and their possible role in forcing the QBO in the equatorial stratosphere (Alexander and Holton 1997). In these experimental studies with regional models, numerical time integrations were performed for short time periods, less than a week, under specific background conditions with idealized mean zonal wind profiles. These studies focus on upward influence from the troposphere to the stratosphere associated with GWMT, without attention to CMT in the troposphere.

There are only a few studies that examined the relationship between CMT and GWMT in the troposphere with a regional cloud-system-resolving model. Recently, Lane and Moncrieff (2010, hereafter LM10) and Shaw and Lane (2013, hereafter SL13) studied the connection between CMT and GWMT in a two-dimensional cloud-system-resolving model with idealized zonal mean zonal wind profiles. In these studies they introduced a linear group velocity criterion to objectively separate CMT from GWMT, assuming that GWMT is typically associated with upward-propagating gravity waves. SL13 showed that the GWMT contribution is present in the troposphere and stratosphere, whereas the CMT contribution forms a large part of the residual (non-upward-propagating contribution) and dominates the fluxes in the troposphere. SL13 also analyzed the vertical sensible heat flux to isolate the effects of unstable convection from upward-propagating gravity waves, and the results support the physical interpretation of the CMT and GWMT contributions.

Downward-propagating gravity waves, as well as upward-propagating ones, are generated by convection. These could be responsible for the vertical momentum transport in the troposphere and also the initiation of a new convective system (e.g., Mapes 1993). As SL13 mentioned, the non-upward-propagating contributions in their analysis could include momentum transport by downward-propagating gravity waves.

In this study, we develop a method to separate the momentum flux in time–space spectral space into three contributions of the upward and downward GWMTs and CMT by extending the works of LM10 and SL13. The method is applied to every 2-day period during the cycle of the QBO-like oscillation to analyze the periodic variation of momentum budget in the self-sustained oscillation. The results give periodic variations of the characteristics of vertical momentum transport not only in the stratosphere but in the troposphere, in association with the QBO-like oscillation of the mean zonal wind.

The remainder of the paper is organized as follows. Section 2 describes the two-dimensional cloud-system-resolving model experiments and diagnostic methodology. The general features of the QBO-like oscillation are also described, including periodic variations of organized convective systems. Section 3 shows the momentum budget of the QBO-like oscillation. Then, section 4 introduces the method to separate the momentum flux into CMT and upward and downward GWMTs and applies it to a time period of 2 days during squall-line type of precipitation. The results of separation applied to another 2-day period during back-building type of precipitation are given in section 5. In section 6, the modulation of the momentum transports in accordance with the QBO-like oscillation is described. Discussion is given in section 7. Finally, section 8 concludes this paper.

2. Cloud-system-resolving model experiments and diagnostics

a. *Cloud-system-resolving model experiments*

1) MODEL DESCRIPTION

The model used here is the Advanced Research version of the Weather Research and Forecasting (WRF) Model (ARW), version 3 (Skamarock et al. 2008), and the model configurations reported here are based on those for the ''Hightop0'' case described by YBN14. The numerical experiment uses a two-dimensional model domain that is 640 km long, with 5-km horizontal grid spacing and 200 vertical levels up to 40 km at the initial state. A periodic boundary condition is assumed in the zonal direction. The Coriolis parameter is set to zero. A Rayleigh damping layer is introduced at the top boundary for 5-km depth to absorb vertically propagating gravity waves by relaxing dependent variables to the reference state given as an initial condition. Yonsei University (YSU) PBL is employed as planetary boundary layer scheme with surface fluxes based on Monin–Obukhov similarity theory, and the 1.5-order prognostic turbulence kinetic energy (TKE) closure option is used for the eddy viscosities. Convective parameterization is turned off. The WRF single-moment 6-class microphysics scheme (WSM6) is used for cloud microphysics to represent explicit moist convection. For radiation schemes, the Rapid Radiative Transfer Model (RRTM) is used for longwave radiation and MM5 (Dudhia) for shortwave radiation. We set the solar declination to the equinox condition and fix the solar insolation to the daily averaged value.

An idealized zonally uniform initial condition is given by the climatological profiles of temperature and moisture on the equator that were created from the ERA-Interim dataset (Dee et al. 2011). The imposed zonal wind is $5\,m\,s^{-1}$ below 11 km, $0\,m\,s^{-1}$ above 16 km, and merges smoothly between them. At the bottom boundary, the sea surface temperature (SST) is uniform, with a constant value of 27°C. Convection is triggered by an initial thermal bubble with horizontal and vertical radii of 50 and 4.8 km, respectively, and a perturbation temperature of 3 K.

We performed time integration for 2 yr with a time step of 10 s. The outputs were sampled at 5-min intervals for the periods between days 260 and 408, during which a quasi-equilibrium state has been already achieved (YBN14). The output variables are zonal and vertical winds, temperature, potential temperature, cloud water mixing ratio, ice mixing ratio, and precipitation.

2) A QBO-LIKE OSCILLATION AND ASSOCIATED MODULATION OF CONVECTIVE SYSTEMS

In the quasi-equilibrium state, the time mean zonal mean temperature (Fig. 1 in YBN14) shows a lapse rate of $7.7\,K\,km^{-1}$ in the troposphere, similar to the observed climatology, and has lower values, about 10 K, than the climatology. The tropopause is located around 13 km, several kilometers below the climatology. A self-sustained oscillation is obtained in this radiative–moist-convective quasi-equilibrium state, and it shows a QBO-like oscillation with a period of 134 days in the stratosphere and associated periodic variations in the troposphere (Fig. 1a). Note that the mean upwelling of the Brewer–Dobson circulation, which can affect the descent rate of the QBO wind shear (e.g., Watanabe and Kawatani 2012), is not present in the two-dimensional model. The downward propagation of the oscillation signal in the zonal mean zonal wind starts from the bottom of the Rayleigh damping layer (~30 km) and reaches to the surface, changing the propagation speed with height. For example, the zero-wind line propagates downward from 30 to 20 km during days 265 and 305 at a mean speed of roughly $250\,m\,day^{-1}$, from 20 to 12.5 km during days 305 and 365 at $\sim 125\,m\,day^{-1}$, and from 12.5 km to the surface during days 300 and 350 at $\sim 250\,m\,day^{-1}$.

Figure 1b shows the zonal mean potential temperature anomaly from the time mean. In the stratosphere, the descent of a warm anomaly with a cold anomaly above is clear in association with that of shear layers separating the easterly and westerly zonal mean zonal winds. In the troposphere, the potential temperature anomalies appear simultaneously through the entire depth, and vary periodically; the warm anomalies appear for days 260–268, 320–340, and 375–400 during which the zero-wind line exists in the middle troposphere at around $z = 2.5$–7.5 km, whereas the cold anomalies appear during the periods when the zero-wind line exists in the upper troposphere or lower stratosphere.

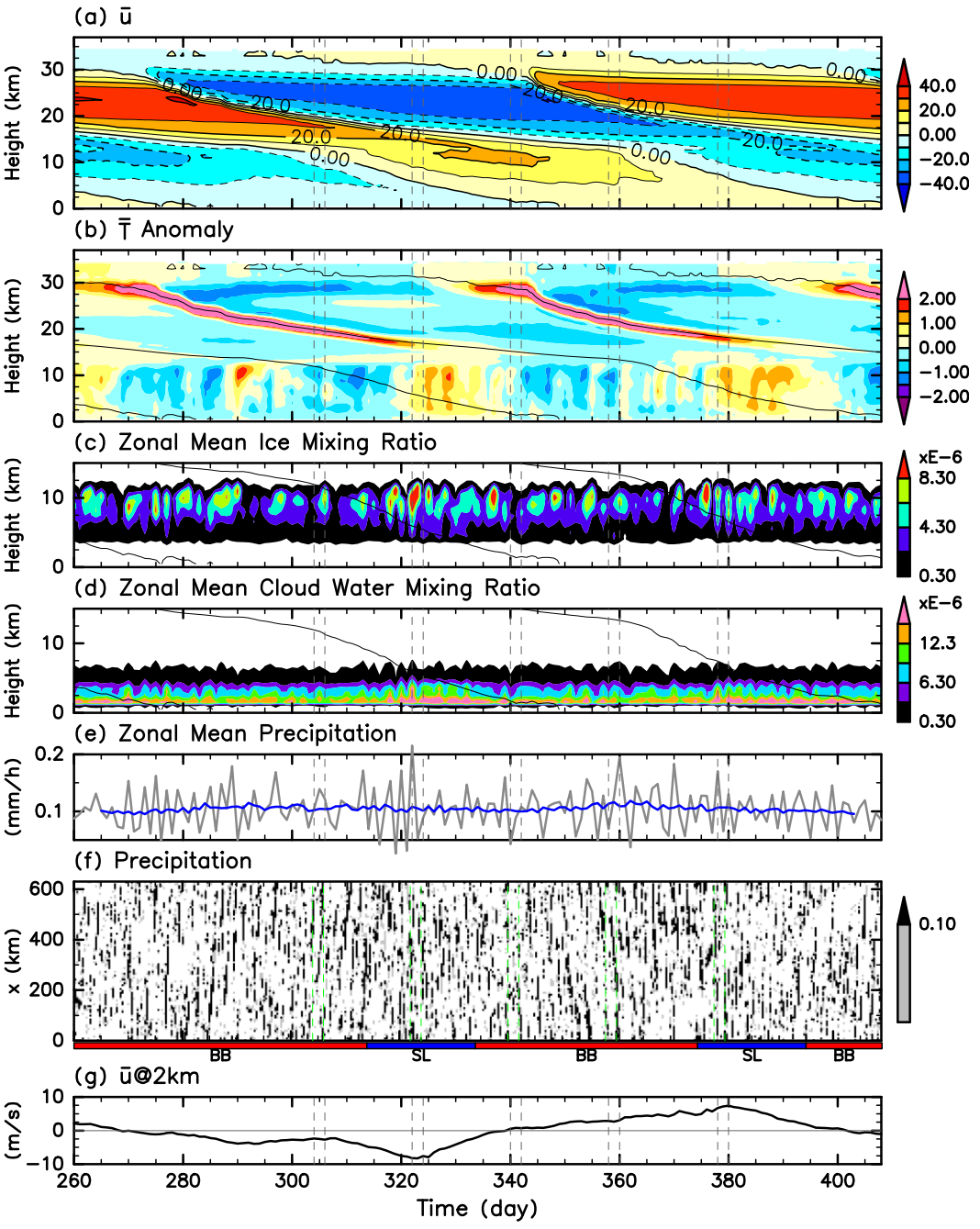

FIG. 1. Time variations of the QBO-like oscillation. Time–height sections of (a) zonal mean zonal wind ($m\,s^{-1}$), (b) zonal mean potential temperature anomaly from the time mean (K), (c) zonal mean ice mixing ratio ($kg\,kg^{-1}$), and (d) zonal mean mixing ratio of cloud water ($kg\,kg^{-1}$); (e) time series of zonal mean precipitation ($mm\,h^{-1}$) and its 21-day running mean (blue line); (f) zonal–time section of precipitation ($mm\,h^{-1}$); and (g) time series of zonal mean zonal wind at $z = 2$ km. Overlaid black contours in (a)–(d) show the zero-wind line of the zonal mean zonal wind. Five pairs of vertical dashed lines show the corresponding 2-day periods presented in Fig. 2. Red and blue bars at the bottom of (f) denote the BB- and SL-type periods, respectively.

Figures 1c and 1d show the ice mixing ratio and the cloud water mixing ratio, respectively. The ice exists above the freezing level and below the tropopause (z = 5–12 km) and has a peak around 10 km, whereas the cloud water exists below the freezing level (z = 0.5–5 km) and has a peak around 2 km. As well as the temperature anomaly, periodic modulation of these cloud variables is discernible and should be related to the

modulation of moist convections; the ice mixing ratio and cloud water mixing ratio increase for days 310–340 and 370–400, during which the zero-wind line exists in the middle troposphere. However, the modulation of the zonal mean precipitation is not very clear because of large fluctuations of high-frequency components (Fig. 1e).

Figure 1f shows a zonal–time section of precipitation. Precipitation is organized into bands that correspond to propagating convective activity. Figure 2 shows the precipitation distributions and the mean flow profiles for five 2-day periods at intervals of about 20 days, as indicated by the vertical dashed lines in Fig. 1. During days 304–305 (Figs. 2a,b), when the zonal mean zonal wind is easterly in the troposphere, each precipitation system propagates westward at the speed of $\sim -6.0\,\mathrm{m\,s^{-1}}$, and a new system emerges at the rear side of the previous one with a mean "group velocity" of $\sim 2.0\,\mathrm{m\,s^{-1}}$. We refer to this type of propagation pattern of precipitation as a back-building (BB) type. During days 322–323 (Figs. 2c,d), when the easterly jet exists in the lower troposphere at $z = 2\,\mathrm{km}$, each precipitation system propagates westward at the speed of $\sim -10\,\mathrm{m\,s^{-1}}$, and a new system emerges at the front side of the old one. We refer to this type of propagation pattern of precipitation as a squall-line (SL) type. During days 340–341 (Figs. 2e,f), the zonal mean zonal wind in the lower troposphere is almost zero, and precipitation is less organized or of a weak BB-type signature. During the last half of the oscillation, when the tropospheric wind profiles are mirror images of those during the first half, the BB and SL types of the precipitation pattern also appear, but the precipitation patterns propagate in the opposite direction (Figs. 2g–j).

Precipitation pattern is modulated in association with the QBO-like oscillation, characterized by alternating between the SL and BB types periodically (shown as blue and red bars, respectively, at the bottom of Fig. 1f). Figure 1g shows that the SL-type periods begin when the zonal mean zonal wind at $z = 2\,\mathrm{km}$ exceeds $\sim 5\,\mathrm{m\,s^{-1}}$ and end when it slows to less than $\sim 2.5\,\mathrm{m\,s^{-1}}$. The zonal mean variables related to moist convections, such as the tropospheric temperature, ice mixing ratio, and cloud water mixing ratio, have positive anomalies during the SL-type periods, whereas negative anomalies during the BB-type periods, as shown in Figs. 1b–d.

b. *Diagnostics*

1) MOMENTUM BUDGET

In a two-dimensional (x–z) periodic system without the rotation of the earth, the tendency equation for the zonal mean zonal wind $\overline{u}(z, t)$ can be given by

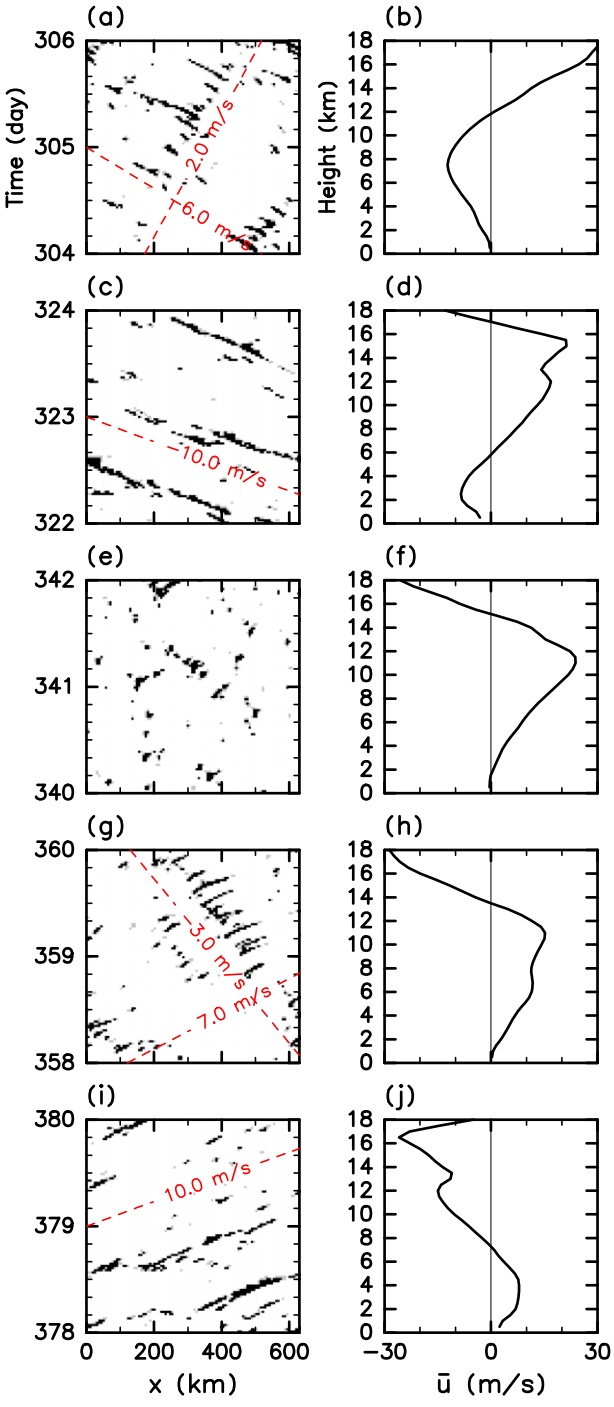

FIG. 2. (left) Zonal–time sections of precipitation ($\mathrm{mm\,h^{-1}}$) for 2-day time interval. (right) The 2-day averaged zonal mean zonal wind ($\mathrm{m\,s^{-1}}$) for $0 \le z \le 18\,\mathrm{km}$. (a),(b) Days 304–305 (BB type); (c),(d) days 322–323 (SL type); (e),(f) days 340–341 (BB type); (g),(h) days 358–359 (BB type); and (i),(j) days 378–379 (SL type). Red dashed lines show constant phase speeds for each value.

$$\frac{\partial \overline{u}}{\partial t} = -\frac{1}{\rho_0(z)}\frac{\partial F_z}{\partial z} + \text{residual}, \quad (1)$$

where $F_z(z, t) = \rho_0(z)\overline{u'w'}$ is the zonal mean vertical flux of horizontal momentum; $\rho_0(z)$ is the background density; u and w are the horizontal and vertical winds, respectively; and the overbar and prime denote the zonal mean and anomaly from the zonal mean, respectively. The residual consists of turbulent mixing and implicit numerical diffusion.

2) Upward- versus non-upward-propagating waves

As written in section 1, the vertical flux of horizontal momentum includes contributions from CMT and upward and downward GWMTs. First, the upward- and non-upward-propagating contributions are separated using the method that was introduced in LM10 and used in SL13. Then, in section 4, we introduce a new method to subtract the contribution related to convective circulations from the upward- and non-upward-propagating contributions.

LM10 and SL13 used a filter in spectral space that isolates the upward and nonupward contributions. This filter is derived based on the linear theory of gravity waves and the so-called Eliassen–Palm (EP) theorem (Eliassen and Palm 1961; Lindzen 1990); that is,

$$\overline{p'w'} = \rho_0(c - \overline{u})\overline{u'w'} = \rho_0 c_{g_z}\overline{E}, \quad (2)$$

where p is the pressure, c is the phase speed in the x direction, c_{g_z} is the vertical component of group velocity, and E is the wave energy per unit mass defined as

$$E = \frac{|\mathbf{v}'|^2}{2} + \frac{g\theta'^2}{2\overline{\theta}\left(\frac{d\overline{\theta}}{dz}\right)}, \quad (3)$$

where θ is the potential temperature, g is the magnitude of gravity, and $\mathbf{v}' = (u', w')$. Spectral components were derived by a two-dimensional Fourier transform in the horizontal space and time coordinates at every vertical level. Spectral components that have a positive group velocity ($c_{g_z} > 0$) represent upward-propagating waves. The remaining spectral components represent the non-upward-propagating contribution, which is regarded as momentum transport by convection and downward-propagating gravity waves. LM10 used the relationship between the sign of the vertical flux of horizontal momentum $\rho_0\overline{u'w'}$ and the intrinsic phase speed $c - \overline{u}$ to separate the spectral components, whereas SL13 used the sign of the pressure flux $\overline{p'w'}$.

We use the spectrum of the momentum flux multiplied by the intrinsic phase speed to separate the spectral components into upward- and non-upward-propagating contributions. The spectrum of the momentum flux is calculated by multiplying the cospectrum of the horizontal and vertical components of wind anomaly from the zonal mean by the background density. The sign of each spectral component is used as a filter in spectral space that isolates the upward and nonupward contributions. However, as convection and gravity waves can coexist in the domain at the same time, the separation using a criterion of the linear wave theory may not be perfect to separate CMT from GWMT.

3. Momentum budget

Figures 3a–c show time–height sections of each term in Eq. (1). In the stratosphere, most of the acceleration of the zonal mean zonal wind occurs in a confined layer of about 5 km around the zero-wind line for a limited time interval of about 5 days (Fig. 3a). Easterly acceleration ($\partial\overline{u}/\partial t < 0$) begins around the altitude of 30 km on day 270 and propagates downward along with the zero-wind line with easterly shear ($\partial\overline{u}/\partial z < 0$). The westerly acceleration ($\partial\overline{u}/\partial t > 0$) begins around 30 km on day 340 and propagates downward along with the zero-wind line with westerly shear ($\partial\overline{u}/\partial z > 0$). A similar feature is found in the convergence term of the vertical flux of horizontal momentum $C_{F_z}(z, t)$, but its vertical position is shifted upward in comparison to the acceleration term of the zonal mean zonal wind (Fig. 3b). The residual component is large at around 2 km above and below the zero-wind line (Fig. 3c); there is a positive peak above and a negative peak below the zero-wind line with easterly shear, whereas a negative peak above and a positive peak below the zero-wind line with westerly shear. These dipoles of the residual component cancel the upward shift of the convergence term of the vertical flux of horizontal momentum.

The dipoles of residual component could be caused by vertical mixing around the zero-wind lines where the vertical shear of the zonal mean zonal wind is large (e.g., Geller et al. 1975). Because the model outputs of this experiment did not include the subgrid TKE, we estimate the local Richardson number (Ri) [$\mathrm{Ri}(x, z, t) = (g/\theta)(\partial\theta/\partial z)(\partial u/\partial z)^{-2}$] from the output data. Figure 3e shows percentage of grid boxes that satisfy $\mathrm{Ri} < 0.25$ at each level and each time. The grid boxes that satisfy $\mathrm{Ri} < 0.25$ exist only around the zero-wind lines in the stratosphere, suggesting vertical turbulent mixing due to gravity wave breaking around there. The percentage

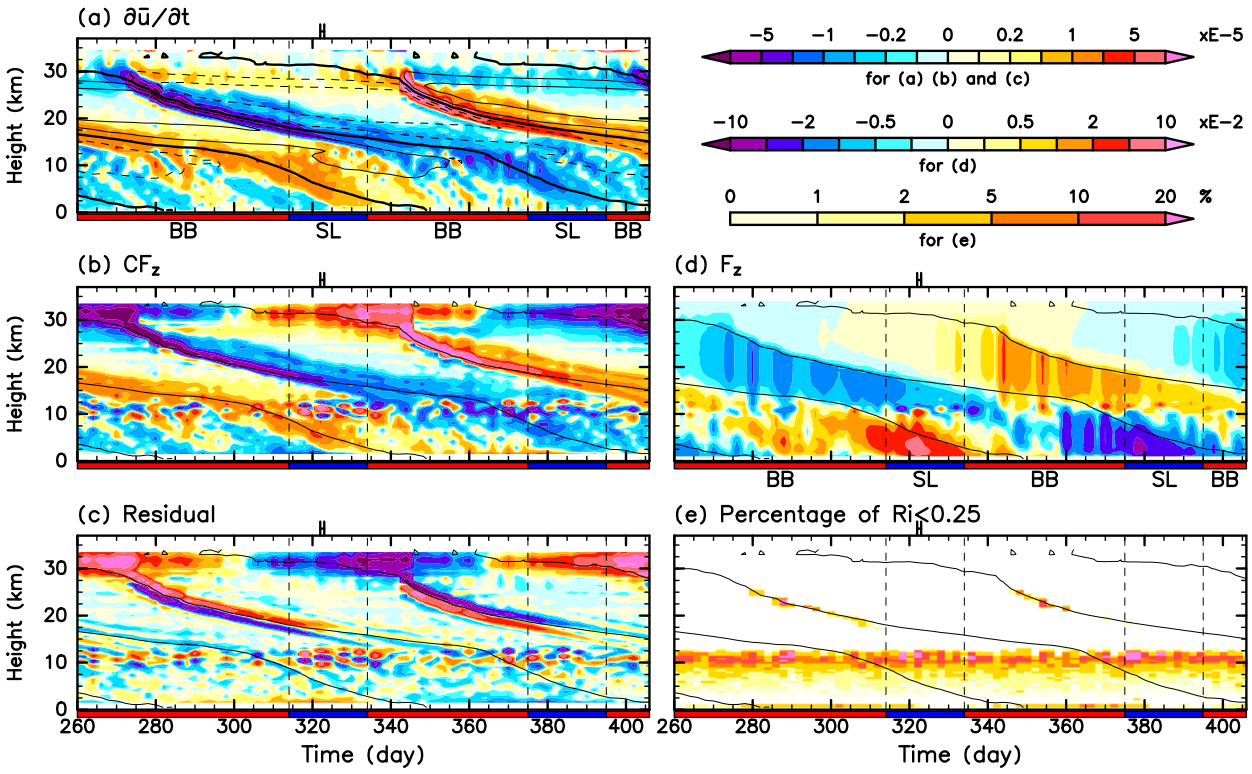

FIG. 3. Time–height sections of each term in Eq. (1): (a) acceleration of the zonal mean zonal wind ($\partial\overline{u}/\partial t$), (b) convergence of the vertical flux of horizontal momentum (i.e., C_{F_z}), and (c) residual term. Time–height sections of (d) the zonal mean vertical flux of horizontal momentum (i.e., F_z) and (e) percentage of grid boxes that satisfy Ri < 0.25. Values in (a)–(d) are 2-day averaged values. Values in (e) are maximum values at every 2-day period. Overlaid contours in (a) show the zonal mean zonal wind with contour intervals of 15 m s^{-1} with negative values in dashed contours; only the enhanced zero-wind line is shown in (b)–(e). Red and blue bars at the bottom of each plot denote the BB- and SL-type periods, respectively.

is mostly less than 2%, and the maximum percentage is about 25% located at the level of $z = 23$ km. Such vertical mixing of horizontal momentum can produce the dipoles of the residual component, whose signs depend on the sign of the vertical shear (Fig. 3c). The existence of a cold anomaly above a warm anomaly, which is independent of the sign of the vertical shear, around the zero-wind lines in Fig. 1b is also consistent with the vertical turbulent mixing of potential temperature. In the Rayleigh damping layer above 30 km, the residual term almost cancels the convergence term of the vertical flux of horizontal momentum to reduce the acceleration term to a small value by the Rayleigh damping through the oscillation cycle.

In the troposphere, the acceleration of the zonal mean zonal wind occurs rather simultaneously in a wide range of heights between the tropopause ($z \sim$ 13 km) and about 2 km below the zero-wind lines and has a weaker peak around the zero-wind lines than in the stratosphere (Fig. 3a). During the SL-type periods, stronger acceleration occurs in the middle troposphere when the zero-wind line exists there. The convergence term of the vertical flux of horizontal momentum displays a similar feature to the acceleration term of the zonal mean zonal wind (Fig. 3b). Around the tropopause, $z = 10$–15 km, there are two or three layers of strong convergence and divergence, which persist for about 5 days, after which new ones immediately appear. These features are more evident during the SL-type periods, and similar features of opposite sign are found in the residual component (Fig. 3c). Below the altitude of 2 km, there are large values in the convergence and residual terms, especially during the SL-type periods, when the mean zonal wind jet exists around $z = 2$ km with a large wind shear near the surface (see Figs. 2d,j). The percentage of the grid boxes that satisfy Ri < 0.25 is large in the upper troposphere and near the surface (Fig. 3e), suggesting instability around there. The peak value is about 30% and is located around the tropopause, $z =$ 10–12 km, where the two or three layers of large

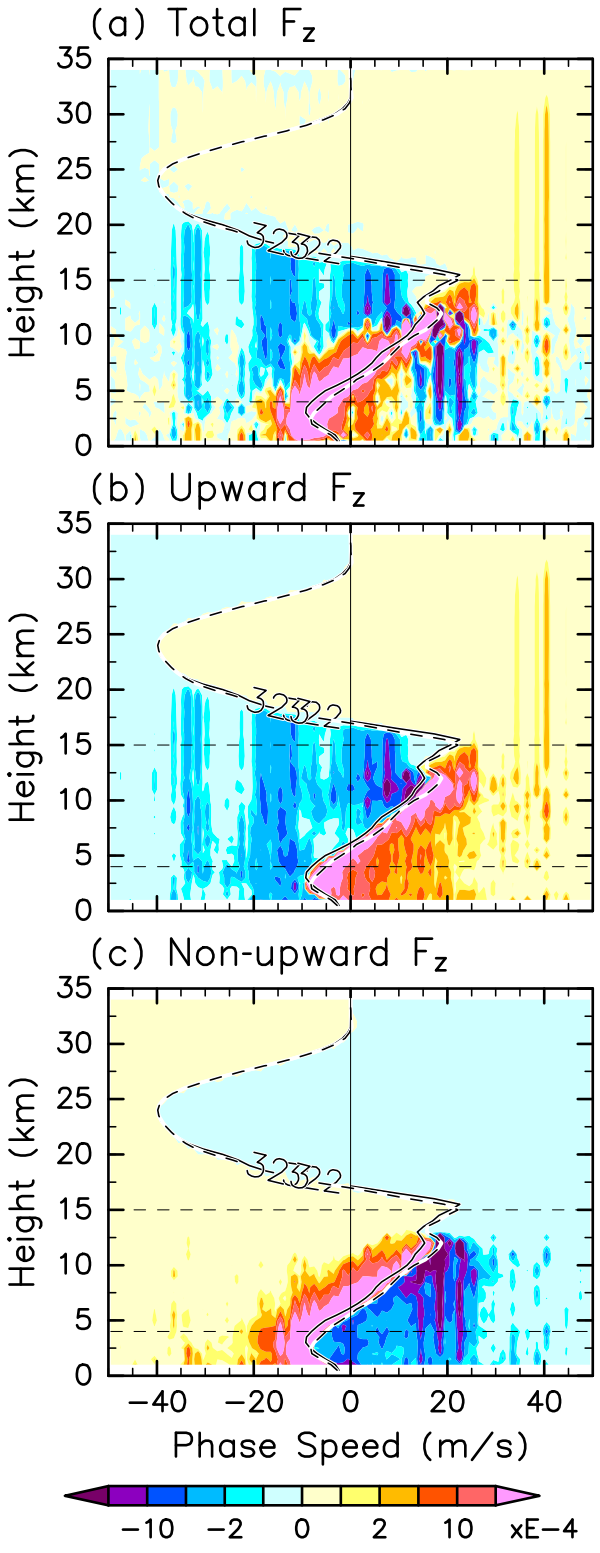

FIG. 4. Phase speed spectra of the vertical flux of horizontal momentum for all heights z for days 322–323: (a) total flux, (b) the spectra separated into the upward-propagating contribution, and (c) the spectra separated into the non-upward-propagating contribution. Spectral unit is $\mathrm{kg\,m^{-1}\,s^{-2}\,(m\,s^{-1})^{-1}}$. Solid and dashed black lines show zonal mean zonal winds on day 322 and day 323, respectively.

negative and positive values exist in the convergence term (Fig. 3b) and in the residual component (Fig. 3c).

Figure 3d shows a time–height section of the vertical flux of horizontal momentum [i.e., $F_z(z, t)$]. The momentum flux is basically positive when the zonal mean zonal wind is easterly, whereas it is negative when the mean zonal wind is westerly. In the stratosphere, the momentum flux is large between the tropopause and the zero-wind lines, around which the mean zonal wind has a large vertical shear. The momentum flux is relatively small in the stratosphere during the SL-type periods, compared with the BB-type periods. It amplifies suddenly in the depth between the tropopause and the zero-wind lines at the time when large acceleration of the zonal mean zonal wind starts near the bottom of Rayleigh damping layer. In the troposphere, the momentum flux is large between the surface and around the zero-wind lines, especially during the SL-type periods. The momentum flux is positive (i.e., the upward flux of the eastward momentum) during days 280–335, when the precipitation pattern propagates westward (see Figs. 2a,c), whereas the momentum flux is negative during days 340–395, when the precipitation pattern propagates eastward (see Figs. 2e,g,i).

4. Method of separating CMT from GWMTs and its application for an SL-type period

a. Time–space spectral analysis separating upward- and non-upward-propagating components

As stated above, the vertical flux of horizontal momentum is associated with CMT and upward and downward GWMTs. In this section, we introduce a method of separating the vertical flux into the three contributions using time–space Fourier separation, applying it to a 2-day time period during an SL type, as an example, when the zonal mean variables related to moist convection and the acceleration of the zonal mean zonal wind are large in the troposphere (Figs. 1b–d and 3a). Figure 4a shows the phase speed spectra of the vertical flux of horizontal momentum $[\rho_0(z)\overline{u'w'}]$ for all heights z for days 322–323. To create this plot, the momentum flux spectrum was computed for zonal wavenumber k and frequency ω using the cospectrum of the horizontal and vertical components of wind anomaly from the zonal mean, and each spectral element for k and ω was sorted into phase speed $c = \omega/k$ bins of $1\,\mathrm{m\,s^{-1}}$ width. The spectra were calculated at 0.5-km vertical intervals. During this period, the spectra have a positive peak in

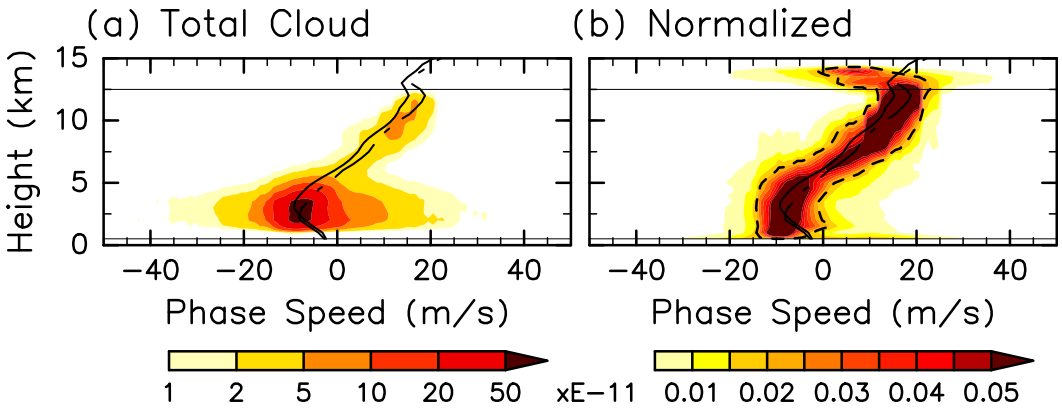

FIG. 5. Phase speed spectra of (a) the total cloud mixing ratio (cloud water plus ice) for the height range of $0 \le z \le 15$ km for days 322–323 and (b) normalized spectra at each level. Dashed line in (b) denotes 98% range.

the troposphere, with small intrinsic phase speeds [$c \sim \overline{u}(z)$]. In the stratosphere, the momentum flux is mostly negative for negative intrinsic phase speeds [$c < \overline{u}(z)$] and mostly positive for positive intrinsic phase speeds [$c > \overline{u}(z)$], consistent with the upward propagation of gravity waves [$c_{g_z} > 0$ as given by Eq. (2)]. In the troposphere, on the other hand, the spectra also have a negative peak at the phase speed around 20 m s^{-1}—that is, a positive intrinsic phase speed, suggesting the existence of downward propagation of gravity waves ($c_{g_z} < 0$).

Next, we apply the separation of the vertical flux of horizontal momentum using the upward-wave-propagation criteria from the linear theory of gravity waves, as described in section 2b. Figures 4b and 4c show the separated momentum fluxes of upward- and non-upward-propagating contributions, respectively, using the relationship between the sign of the momentum flux and the intrinsic phase speed as given by Eq. (2)—the same sign for upward-propagating components and the opposite sign for non-upward-propagating components. The upward-propagating contribution shows that the momentum transport signals exist from the lower or middle troposphere to critical levels in the stratosphere, with peak phase speeds of $c \sim 40$, 7, -15, and -33 m s^{-1}. The non-upward-propagating contribution is confined to the troposphere. The downward-propagating signal from the middle troposphere to the surface is clear, with the negative peak of positive intrinsic phase speeds around $c \sim 18$ m s^{-1}. The large positive momentum flux with small intrinsic phase speeds [$c \sim \overline{u}(z)$] in the troposphere in Fig. 4a is separated into the upward- and non-upward-propagating contributions, even though it should be regarded as CMT associated with slantwise convective structures.

b. Separation of convective momentum transport

To separate the momentum flux associated with convective circulations, we first conduct a time–space spectral analysis of the total cloud (cloud water and ice) mixing ratio for the same time period in order to characterize cloud motions. Figure 5a shows the phase speed spectra of the total cloud mixing ratio for the height range of $0 \le z \le 15$ km for days 322–323. The spectral power is large for the range of $0.5 \le z \le 12.5$ km, with two peaks at $z = 2$ and 10 km that correspond to the peak heights of cloud water and ice, respectively. Figure 5b shows the normalized phase speed spectra of the total cloud mixing ratio, which is calculated by dividing the original spectra by the sum of the spectra at each level. The normalized spectra are nearly symmetric about the phase speed equal to the background mean zonal wind $\overline{u}(z)$, which means that clouds are fundamentally steered by background wind at each level. The phase speed range containing 98% of the spectral power (denoted by dashed lines) is located around $\overline{u}(z) \pm 7$ m s^{-1} at each level between $z = 0.5$ and 12.5 km (denoted by thin horizontal lines in Fig. 5). As a criterion to separate CMT from upward and downward GWMTs, we determined this value by trial and error to reduce the contamination by gravity waves in CMT contribution. Most of the results are insensitive to the choice of that value at least for the range of 95%–99%. After subtracting spectral elements whose phase speeds are within this criterion, we regard the remaining spectral components of upward- and non-upward-propagating contributions as the upward and downward GWMTs, respectively.

Figures 6a, 6d, and 6g show the phase speed spectra of the upward GWMT, CMT, and downward GWMT, respectively, for all heights. CMT is confined to the

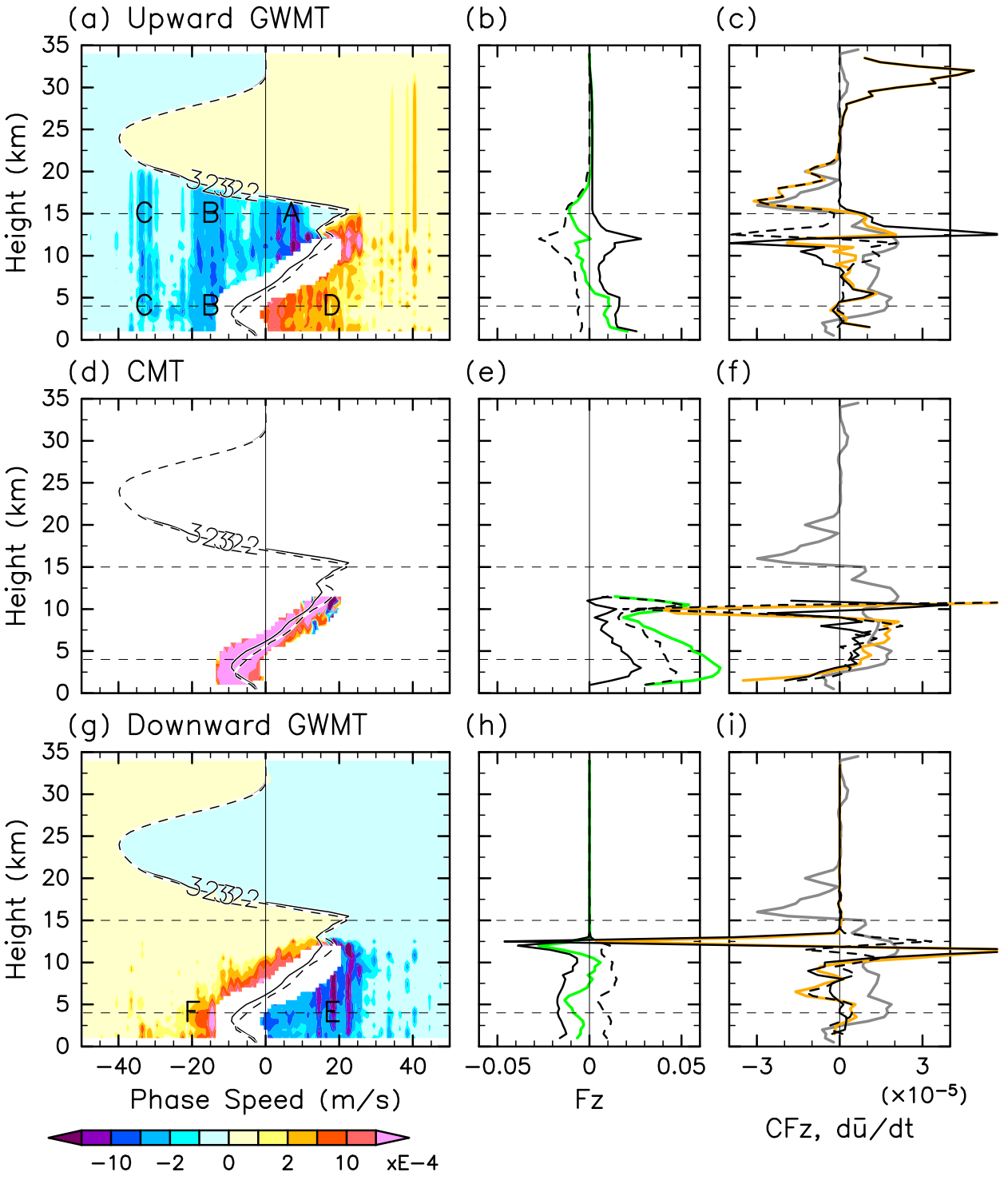

FIG. 6. (left) Phase speed spectra of (a) upward GWMT, (d) CMT, and (g) downward GWMT for all heights for days 322–323. (center) Integral of the vertical flux spectra for (b) upward GWMT, (e) CMT, and (h) downward GWMT over the total phase speeds (green solid line) and over the positive ($c-\bar{u}>0$; black solid line) and negative ($c-\bar{u}<0$; black dashed line) intrinsic phase speeds. (right) The vertical convergence of the integral of the vertical flux spectra for (c) upward GWMT, (f) CMT, and (i) downward GWMT, together with the acceleration of the zonal mean zonal wind (gray line). The convergence of the flux integrated over the total phase speeds is shown as orange line.

troposphere as defined and is mostly positive. The CMT spectra are nearly symmetric about the intrinsic phase speed with respect to the background wind speed $\overline{u}(z)$. The subtraction of the CMT contributions clarifies that there is an upward GWMT at a phase speed of about $c \sim 18\,\mathrm{m\,s^{-1}}$ (marked D in the figure) within the troposphere, which is not propagating into the stratosphere because of the critical level, in addition to the upward GWMTs at the aforementioned peak phase speeds of $c = 7$, -15, and $-33\,\mathrm{m\,s^{-1}}$ (marked A, B, and C, respectively). The spectra for the downward GWMT also show another peak phase speed at $c = -20\,\mathrm{m\,s^{-1}}$ (marked F) in addition to the aforementioned peak phase speed of $c = 18\,\mathrm{m\,s^{-1}}$ (marked E). The figures suggest that the upward GWMT corresponding to A occurs from the top of clouds, whereas the upward GWMTs corresponding to B and C and the downward GWMTs corresponding to E and F are from the middle of clouds.

Figure 6 (center) shows the integral of the vertical flux spectra of the horizontal momentum over the negative ($c - \overline{u} < 0$; black dashed line) and positive ($c - \overline{u} > 0$; black solid line) intrinsic phase speeds, together with the total flux (green line). Figure 6 (right) also shows their vertical convergence (i.e., C_{F_z}; the convergence of the total flux is shown by the orange line), together with the acceleration of the zonal mean zonal wind (gray line). The easterly wind acceleration ($\partial\overline{u}/\partial t < 0$) occurs in the easterly shear layer ($\partial\overline{u}/\partial z < 0$) in the lower stratosphere, centered at $z = 16\,\mathrm{km}$, and the westerly wind acceleration ($\partial\overline{u}/\partial t > 0$) occurs in the westerly shear layer ($\partial\overline{u}/\partial z > 0$) of the troposphere in the height range of $2.5 \le z \le 15\,\mathrm{km}$. The upward GWMT associated with the negative intrinsic phase speeds is larger in magnitude than that with the positive intrinsic phase speeds in the upper troposphere and lower stratosphere, and its divergence ($C_{F_z} < 0$) near the critical levels contributes to the easterly wind acceleration in the lower stratosphere. Note that the vertical position of the divergence is shifted upward in comparison to the wind acceleration, as seen in Fig. 3. Although the upward GWMT in the stratosphere associated with the positive intrinsic phase speeds is small, the flux around the phase speed of $c = 40\,\mathrm{m\,s^{-1}}$ propagating from the upper troposphere results in the large convergence ($C_{F_z} > 0$) in the Rayleigh damping layer above $z = 30\,\mathrm{km}$. The CMTs associated with both of the negative and positive intrinsic phase speeds have positive values, and their convergence in the troposphere contributes to the westerly wind acceleration. In addition, there is large convergence and divergence of the CMT and the downward GWMT around the tropopause ($z = 10$–$12.5\,\mathrm{km}$), as seen in Fig. 3b. The downward GWMT associated with the positive intrinsic phase speeds exceeds that associated with the negative intrinsic phase speeds. The convergence of the downward GWMT has little contribution to the acceleration of the zonal mean zonal wind in the troposphere.

c. *Gravity waves in physical space*

Figure 7a shows an x–t cross section of the vertical wind at $z = 15\,\mathrm{km}$ in the lower stratosphere, where the upward GWMT contribution dominates (Fig. 6), above a convectively active area of $250 \le x \le 500\,\mathrm{km}$. The vertical wind is separated into the upward GWMT, CMT, and downward GWMT contributions, respectively, by being applied the time–space Fourier separation and then transformed into physical space. Figures 7b–d give x–t cross sections of the separation of the vertical wind at $z = 4\,\mathrm{km}$ in the middle troposphere. Figures 7a and 7b show waveforms propagating at the phase speeds of $c = 7$ (A), -15 (B), and -33 (C) $\mathrm{m\,s^{-1}}$ in the lower stratosphere and $c = 18$ (D) and -33 (C) $\mathrm{m\,s^{-1}}$ in the middle troposphere. These phase speeds are close to the peaks in the upward GWMT spectra (Fig. 6a) and are marked with the same symbols. Figure 7d also shows waveforms propagating at the phase speeds close to the peaks in the downward GWMT spectra (Fig. 6g): $c = 18$ (E) and -20 (F) $\mathrm{m\,s^{-1}}$. Figure 7c shows that strong updrafts related to CMT are confined within the cloud while downdrafts exist on either side of the updrafts, consistent with what we expect for convective circulation. A waveform propagating at the phase speed of $c = -7$ (G) $\mathrm{m\,s^{-1}}$ can be discernible in this plot, and this phase speed is a very low intrinsic phase speed for $\overline{u} = -8\,\mathrm{m\,s^{-1}}$ at this level.

Figures 8a–c show instantaneous x–z sections of the vertical wind at $t = 2{:}45$ on day 322 (the time marked by a triangle and a horizontal solid line in Fig. 7) that comprise deep convection in the troposphere around $x = 400\,\mathrm{km}$; each panel shows the separation of the vertical wind into the upward GWMT, CMT, and downward GWMT contributions. The deep convection tilts eastward with height (i.e., in the same sense as the shear vector of the zonal mean zonal wind as shown in Fig. 8d) and has an anvil-like structure extending eastward.

Figure 8a exhibits upward energy-propagating disturbances of the vertical wind around the convection system, which correspond to the waveforms mentioned in Figs. 7a and 7b (marked with the same symbols A, B, C, and D in the figure). The disturbance corresponding to A is located directly above the convection system, showing a westward tilt with height. The disturbances corresponding to B and C exist in the western part of the convection system, from the middle troposphere to the

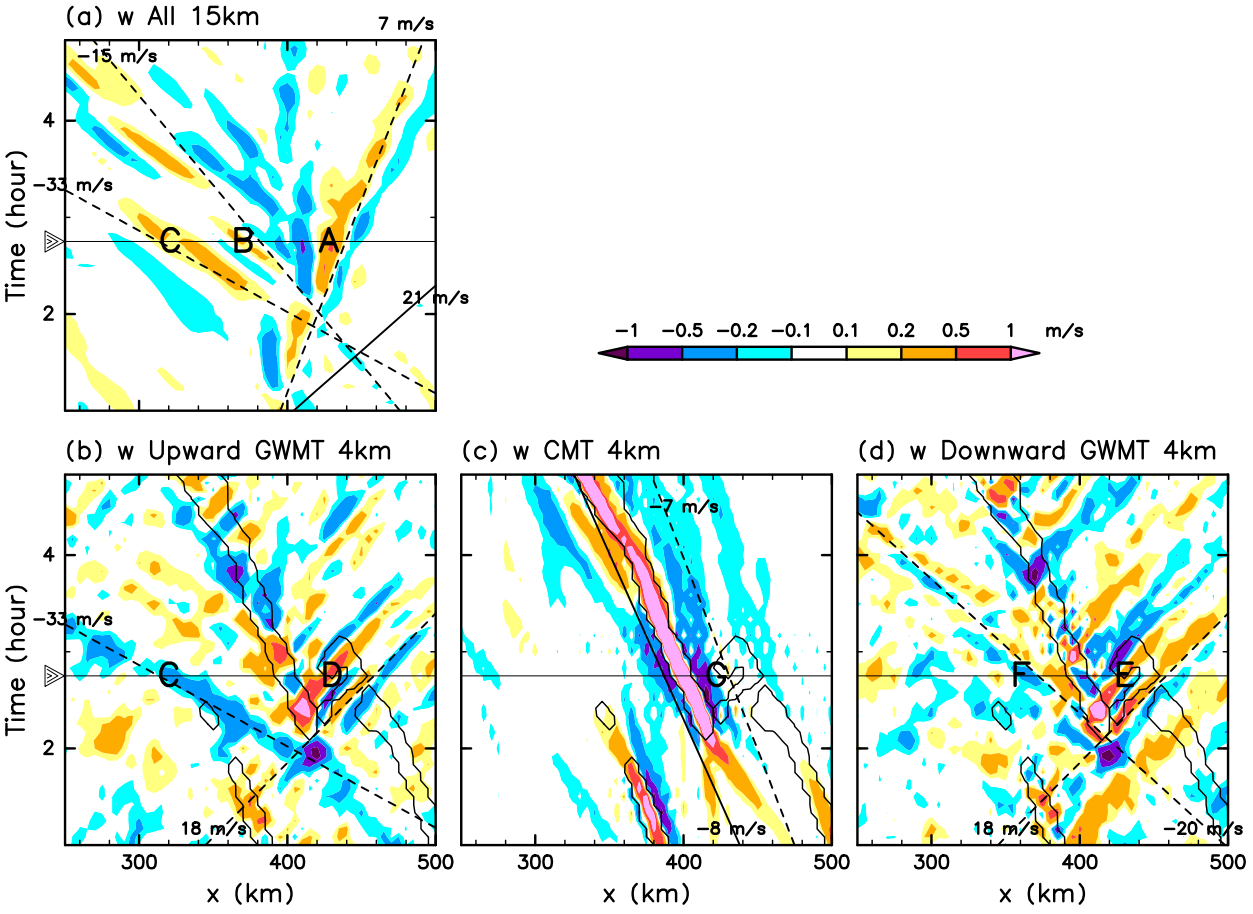

FIG. 7. Zonal–time cross sections of (a) the vertical wind at 15 km for $250 \le x \le 500$ km, $1{:}00 \le t \le 5{:}00$ on day 322, and the vertical wind at 4 km related to (b) upward GWMT, (c) CMT, and (d) downward GWMT. Black contour depicts the cloud boundary at 4 km (mixing ratio >0.01 g kg^{-1}). Dashed lines in (a)–(d) show phase speed lines as denoted. Solid black lines in (a) and (c) show phase speed lines equal to the background wind 21 and -8 m s^{-1}, respectively. Time shown by a triangle and solid line is for the timing of Fig. 8.

lower stratosphere with phase lines tilted westward with height. The tilts of the phase lines in the stratosphere are larger than those in the troposphere because of the difference in the static stability N^2. The upward-propagating disturbances corresponding to A–C reach each critical level in the stratosphere located around $z = 17$–20 km (Fig. 6a). The disturbance corresponding to D exists below the anvil-like structure, showing a slight eastward tilt of phase lines with height.

Downward-propagating disturbances also exist in the middle and lower troposphere as shown in Fig. 8c. They correspond to the waveforms mentioned in Fig. 7d. The disturbance corresponding to E is located below the anvil-like structure in the eastern part of the convection system and shows a slight westward tilt of phase lines with height. The disturbance corresponding to F is located in the western part of the convection system, with an eastward tilt of phase lines with height.

The flow pattern related to the CMT contribution (Fig. 8b) has the same eastward tilt with height as the deep convection, showing the ascending flow from front to rear and the descending flow in the rear inflow to have a large positive momentum flux. The disturbance corresponding to G can be detected in the eastern part of the convection system, showing a slight eastward tilt of phase lines with height.

The horizontal phase speed of linear internal gravity waves is expressed as

$$c = \frac{\omega}{k} = \overline{u}(z) \pm \frac{N}{(k^2 + m^2 + 0.25/H^2)^{1/2}}, \qquad (4)$$

with the sign depending on whether the waves propagate toward the east or west relative to the zonal mean zonal wind $\overline{u}(z)$—that is, positive or negative intrinsic phase speed. In Eq. (4), ω is the frequency; k and m are

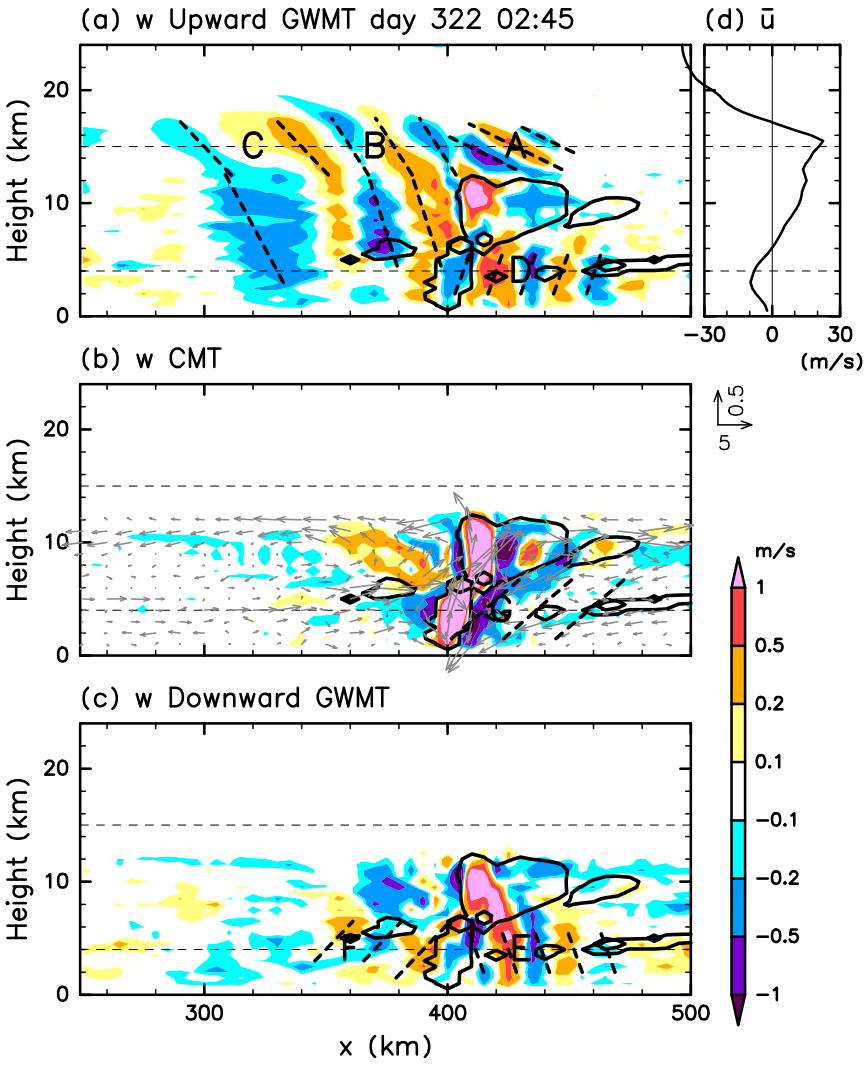

FIG. 8. Zonal–height cross sections of the vertical wind related to (a) upward GWMT, (b) CMT, and (c) downward GWMT at t = 2:45 on day 322. (d) The zonal mean zonal wind at this moment. Vectors in (b) show the perturbations of horizontal and vertical winds from the zonal mean values. Thick black line in (a)–(c) depicts the cloud boundary (mixing ratio >0.01 g kg^{-1}). Black dashed lines in (a)–(c) show wave troughs and ridges.

the horizontal and vertical wavenumbers, respectively; $H = \kappa g/N^2$ is the scale height; and $\kappa = R/c_p$ is the ratio of the gas constant to the specific heat capacity with constant pressure. The mean static stability parameter in this numerical experiment is $1.2 \times 10^{-4}\,\mathrm{s}^{-2}$ in the middle troposphere and $3.7 \times 10^{-4}\,\mathrm{s}^{-2}$ in the lower stratosphere. Using these values and the horizontal and vertical wavelengths ($L_x = 2\pi/k$ and $L_z = 2\pi/m$, respectively) from Fig. 8, we can estimate the horizontal phase speeds c_{est} as listed in Table 1 for waveforms A–G. The last column gives the phase speed c_{obs} read from Fig. 7. As the estimated phase speed c_{est} is in good agreement with the observed one c_{obs} for the waveforms A–F, we can regard that the disturbances of the vertical wind shown in the upward and downward GWMT contributions of Figs. 7 and 8 are the linear internal gravity waves that satisfy the dispersion relationship [Eq. (4)]. On the other hand, the estimated horizontal phase speed of the waveform G is greater than the observed one by about a factor of 3 (Table 1). Therefore, the waveform G could not be recognized as the linear internal gravity wave. These results support the method we introduced here to separate the momentum flux into CMT and upward and downward GWMTs.

TABLE 1. Observed and estimated wave parameters for A–G during days 322–323. The horizontal and vertical wavelengths (L_x and L_z, respectively) are measured from Fig. 8. The estimated phase speed (i.e., c_{est}) is from the dispersion relationship Eq. (4) with the values of N^2 and $\overline{u}$ at 15 km (A–C) and 4 km (D–G), and the phase speed (i.e., c_{obs}) is measured from Fig. 7.

	L_x (km)	L_z (km)	c_{est} (m s^{-1})	c_{obs} (m s^{-1})
A	38	4	6.5	7
B	36	12	−15.9	−15
C	80	18	−34.1	−33
D	27	16	18.3	18
E	27	16	18.3	18
F	40	9	−21.2	−20
G	43	8	−19.6	−7

5. Separation results for a BB-type period

a. *Time–space spectral analysis separating CMT and GWMTs*

Figure 9 shows the phase speed spectra of the total cloud mixing ratio, similar to Fig. 5 but for days 304–305 during a BB-type period. The spectra show similar features as those for an SL-type period (Fig. 5), but the spectral power is smaller in magnitude and the upper peak is located at $z = 8$ km (Fig. 9a). The phase speed range containing 98% of the spectral power is wider and located around $\overline{u}(z) \pm 10$ m s^{-1} (Fig. 9b).

Figure 10 shows the spectra of the upward GWMT, CMT, and downward GWMT, similar to Fig. 6 but for days 304–305. Unlike the SL-type period, the spectra for the CMT (Fig. 10d) are antisymmetric about the intrinsic phase speed with respect to the background wind speed $\overline{u}(z)$; CMT is positive for the negative intrinsic phase speeds, whereas it is negative for the positive ones. The upward GWMT (Fig. 10a) has large contribution for negative intrinsic phase speed with peak phase speeds of $c = -15$ and -25 m s^{-1} (marked "a" and "b" in the figure, respectively) from the middle or lower troposphere to critical levels in the stratosphere. The spectra for the upward GWMT show other phase speed peaks at $c = 5, 15, 25$, and 30 m s^{-1} (marked "c" for $c = 15$ m s^{-1}) in the lower troposphere and is absorbed at the corresponding critical levels in the upper troposphere. The downward GWMT (Fig. 10g) is confined to the troposphere with peak phase speeds of $c = 15$ and -25 m s^{-1} (marked "d" and "e," respectively). In comparison with the SL-type period, the range of the peak phase speeds in the spectra of the upward and downward GWMTs is narrower, as the difference between the background wind speeds in the middle and upper troposphere is smaller.

As seen in gray lines in Fig. 10 (right), the easterly wind acceleration ($\partial\overline{u}/\partial t < 0$) occurs in the easterly shear layer ($\partial\overline{u}/\partial z < 0$) in the lower stratosphere centered at $z = 20$ km, and the westerly wind acceleration ($\partial\overline{u}/\partial t > 0$) occurs in the westerly shear layer ($\partial\overline{u}/\partial z > 0$) in the upper troposphere in the height range of $8 \le z \le 13$ km. The upward GWMT associated with the negative intrinsic phase speeds dominates in magnitude in the upper troposphere and lower stratosphere (Fig. 10b), and its divergence ($C_{F_z} < 0$) near the critical levels contributes to the easterly wind acceleration in the lower stratosphere (Fig. 10c). The vertical position of the divergence is shifted upward compared with the wind acceleration, as seen in Figs. 3 and 10c. Near the tropopause at $z \sim 12.5$ km, the convergence of the upward GWMT associated with the positive intrinsic phase speeds contributes the westerly wind acceleration (Fig. 10c). The CMT is positive for the negative intrinsic phase speeds, whereas it is negative for the positive ones (Fig. 10e). In the upper troposphere, the CMT associated with the negative intrinsic phase speeds and its convergence have the dominant role of the westerly wind acceleration (Figs. 10e,f). The downward GWMT

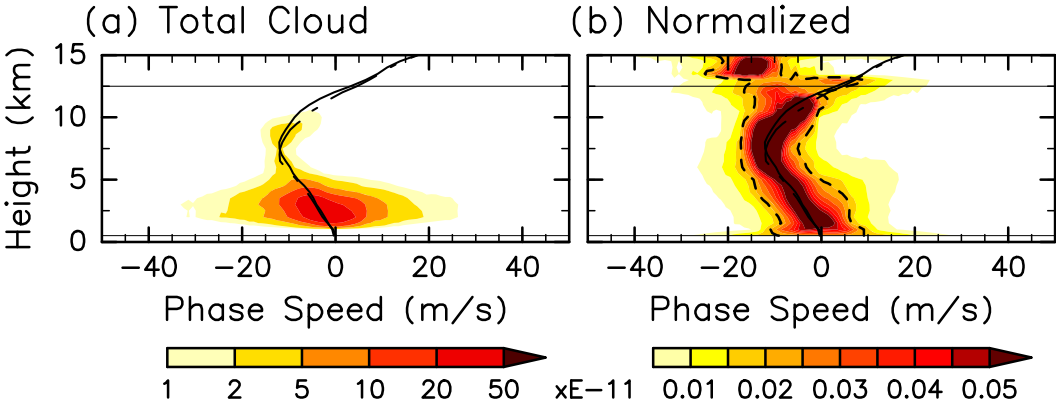

FIG. 9. As in Fig. 5, but for days 304–305.

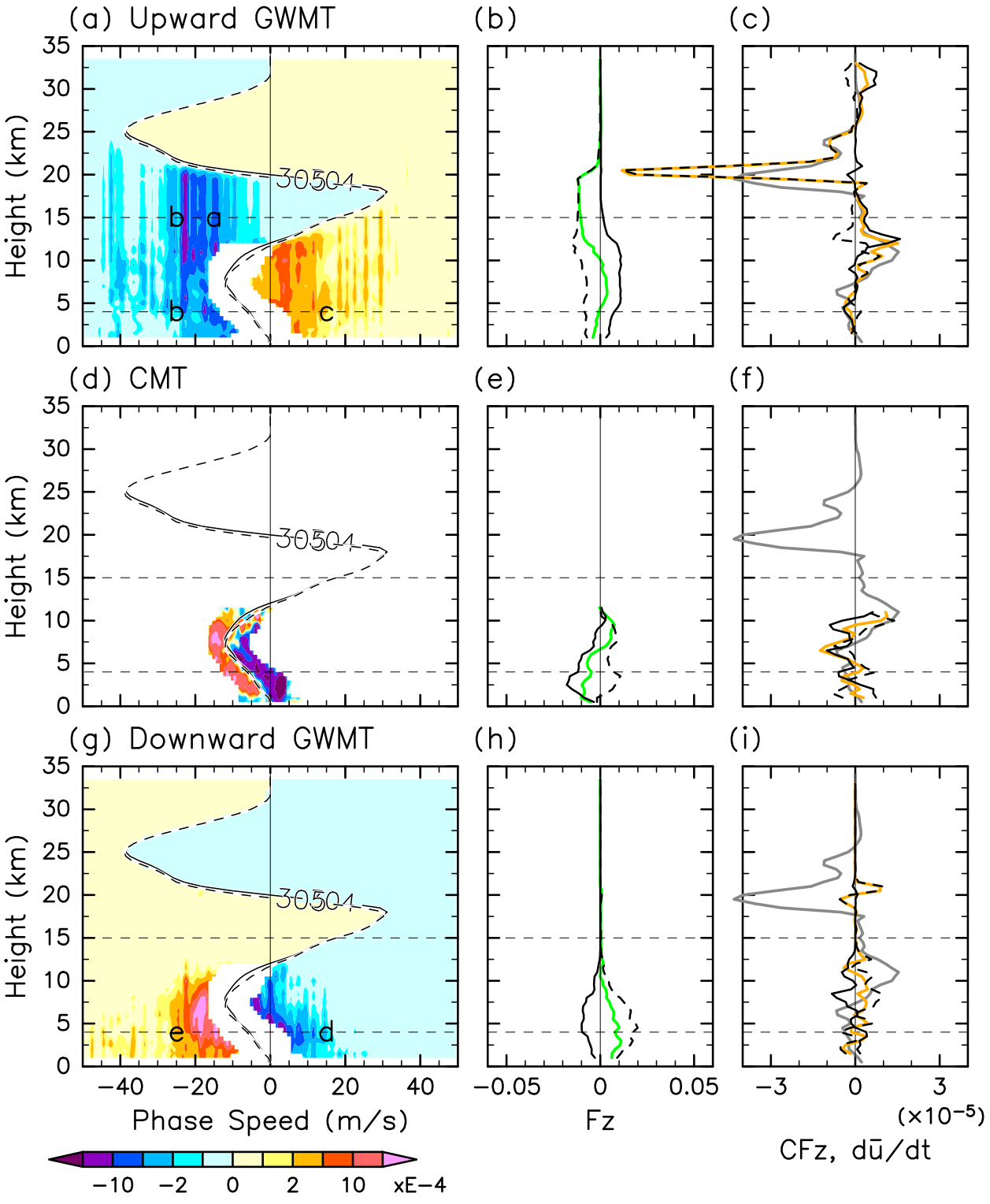

FIG. 10. As in Fig. 6, but for days 304–305.

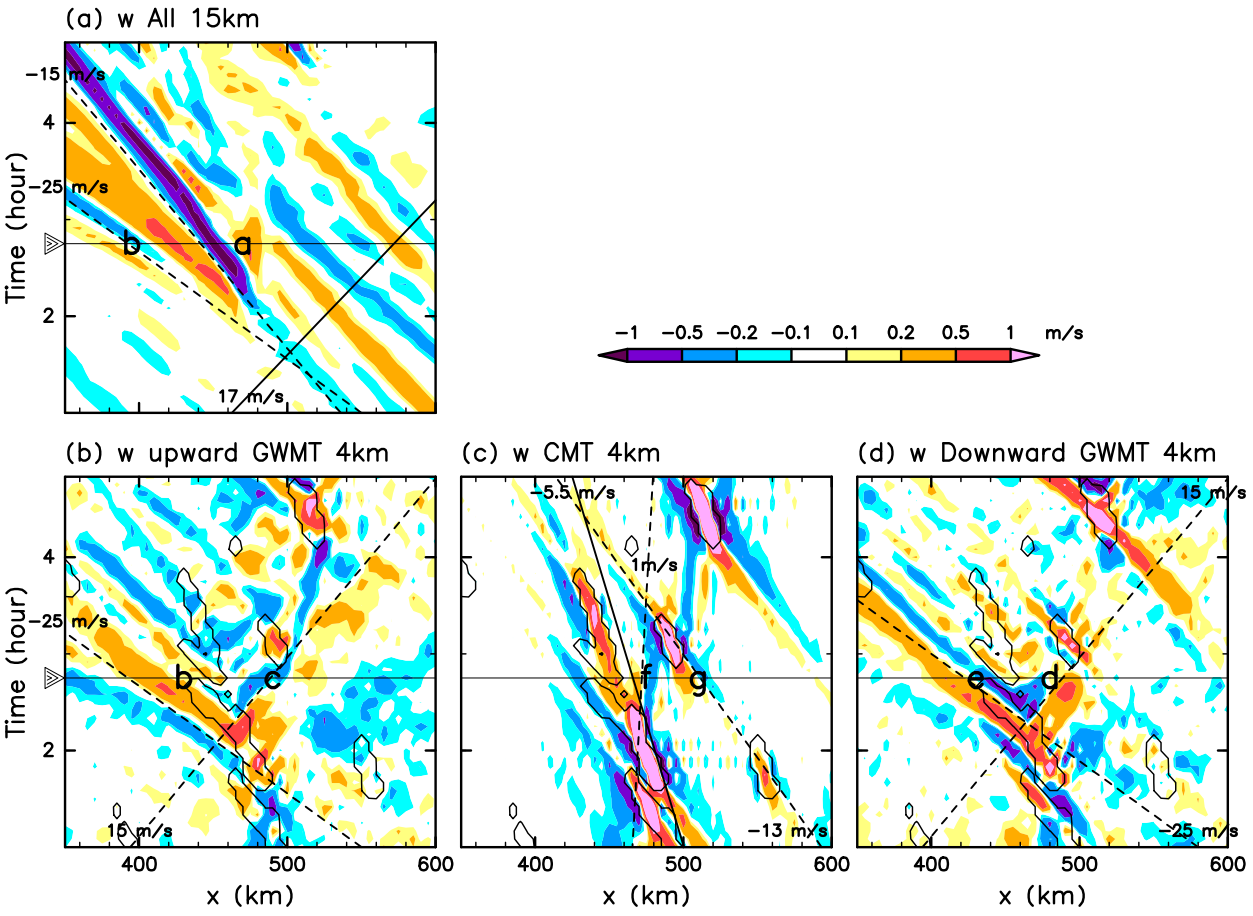

FIG. 11. As in Fig. 7, but for $350 \le x \le 600$ km, 1:00 $\le t \le$ 5:00 on day 304.

associated with the negative intrinsic phase speeds is larger than that associated with the positive intrinsic phase speeds through the troposphere (Fig. 10h). The convergence of the downward GWMT has minor contribution to the acceleration of the zonal mean zonal wind in the troposphere (Fig. 10i), as is the case of the SL-type period (Fig. 6).

b. *Gravity waves in physical space*

Figure 11 shows x–t cross sections of the vertical wind at $z = 15$ km in the lower stratosphere (waveform a) and the separation of the vertical wind into the three contributions at $z = 4$ km in the middle troposphere (waveforms b–d). In the lower stratosphere, waveforms propagate at the phase speeds of $c = -15$ (waveform a) and -25 (waveform b) m s^{-1}, which are close to the peaks in the upward GWMT spectra (Fig. 10a). The vertical wind related to the upward and downward GWMTs (Figs. 11b,d) in the middle troposphere show waveforms propagating at phase speeds close to the peaks in the phase speed spectra (Figs. 10a,g)—for the upward GWMT contribution $c = -15$ (waveform c) and -25 (waveform b) m s^{-1} and for the downward GWMT contribution $c = 15$ (waveform d) and -25 (waveform e) m s^{-1}. The vertical wind related to CMT (Fig. 11c) in the middle troposphere shows strong updraft within the clouds and downdraft on either side of the updraft, as in the case of the SL-type period. In addition, some waveforms propagating at the phase speeds $c = 1$ (waveform f) and -13 (waveform g) m s^{-1}, which are low intrinsic phase speeds, are discernible.

Figure 12 shows instantaneous x–z cross sections of the vertical wind at $t =$ 2:45 of day 304 (the time marked by a triangle and a horizontal solid line in Fig. 11) that constitute a shallow cloud with heights less than 5 km at $x = 430$–450 km with a westward tilt with height, an almost upright deep cloud at $x = 450$–460 km with an anvil-like structure extending eastward, and another shallow cloud with height less than 4 km at $x = 485$–505 km.

Figure 12a shows upward-energy-propagating disturbances of the vertical wind around the convection system, which correspond to the waveforms mentioned in

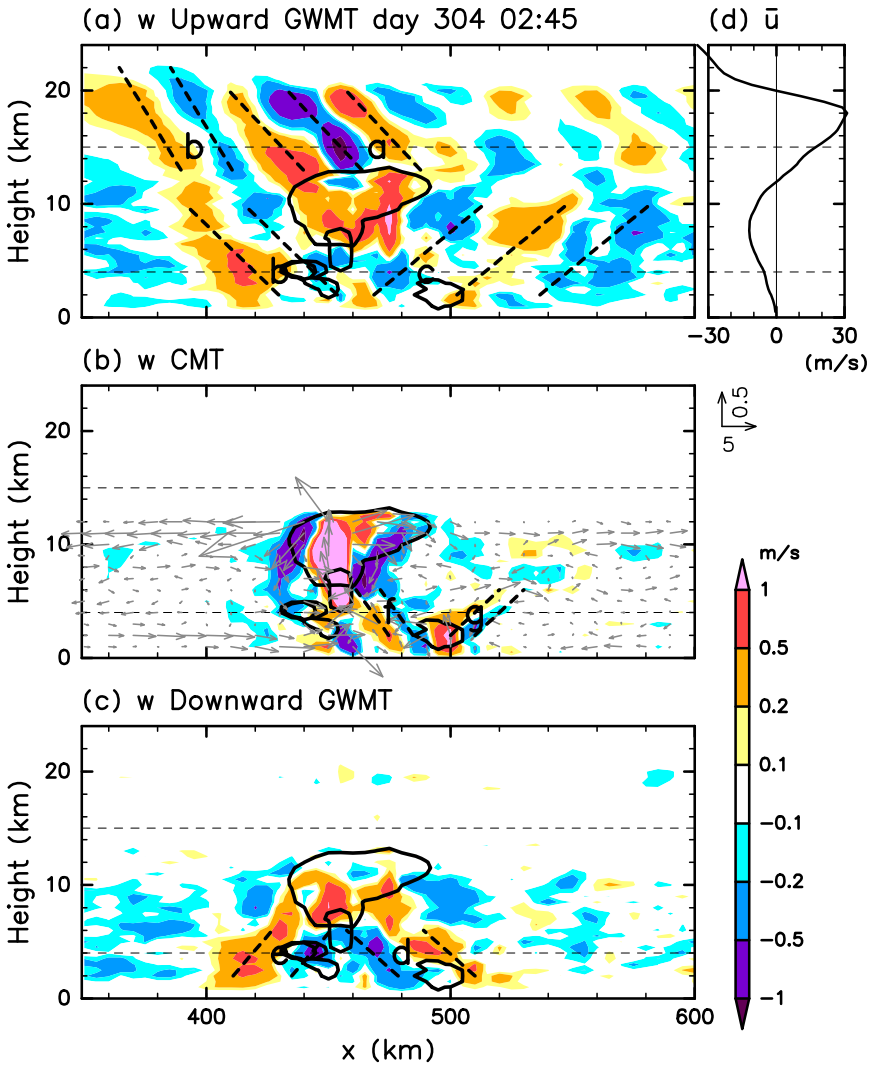

FIG. 12. As in Fig. 8, but for t = 2:45 on day 304.

Figs. 11a and 11b. The disturbance corresponding to waveform a is located above the convection system, showing westward tilt with height. The disturbance corresponding to waveform b exists in the west of the convection system, in the troposphere and stratosphere, with a westward tilt with height. The disturbance corresponding to waveform c is located below the anvil-like structure, with an eastward tilt of phase lines with height.

Downward-propagating disturbances also exist in the middle and lower troposphere as shown in Fig. 12c. They correspond to the waveforms mentioned in Fig. 11d. The disturbance corresponding to waveform d is located in the east of the convection system, with a westward tilt of phase lines with height, and the disturbance corresponding to waveform e is located in the west of the convection system with an eastward tilt with height.

The flow pattern related to the CMT contribution (Fig. 12b) shows anticlockwise and clockwise circulations in the front and rear of the deep convection as the system moves westward. The disturbance corresponding to f is located between the deep cloud around x = 455 km and the shallow cloud around x = 495 km with a westward tilt with height, and the disturbance corresponding to g is located in the east of the shallow cloud with an eastward tilt of phase lines with height.

The horizontal phase speeds estimated by the dispersion relationship [Eq. (4)] for waveforms a–g are listed in Table 2, together with the c_{obs} read from Fig. 12 in the last column. As the estimated phase speed is in good agreement with the observed one for the waveforms a–e, we can regard that the disturbances of the vertical wind shown in the upward and downward

TABLE 2. As in Table 1, but for a–g during days 304–305. Here, L_x and L_z are measured from Fig. 12 and c_{obs} from Fig. 11. The estimated phase speed uses the values of N^2 and $\overline{u}$ at 4 km (c–g) and 15 km (a and b).

	L_x (km)	L_z (km)	c_{est} (m s^{-1})	c_{obs} (m s^{-1})
a	48	11	−14.6	−15
b	42	15	−24.7	−25
c	68	12	14.7	15
d	68	12	14.7	15
e	48	12	−26.0	−25
f	20	6	4.12	1
g	20	4	−12.0	−13

GWMT contributions of Figs. 11 and 12 are the linear internal gravity waves that satisfy the dispersion relationship [Eq. (4)]. For the waveform f in the CMT contribution, the estimated phase speed is greater than the observed one by about a factor of 4, suggesting that the waveform f could not be recognized as the linear internal gravity wave. On the other hand, for the waveform g, the estimated phase speed is in good agreement with the observed one. This indicates that CMT contribution may include inevitable contamination by gravity waves with small intrinsic phase speeds during the BB-type periods.

6. Momentum transports associated with the QBO-like oscillation

The time variation of the vertical momentum transports in accordance with the QBO-like oscillation is examined in Fig. 13. It shows the integral of the phase speed spectra of the vertical momentum flux over all the phase speeds (Fig. 13, top), the positive intrinsic phase speeds ($c - \overline{u} > 0$; Fig. 13, middle), and the negative intrinsic phase speeds ($c - \overline{u} < 0$; Fig. 13, bottom) for the upward GWMT (Fig. 13, left), CMT (Fig. 13, center), and downward GWMT (Fig. 13, right) contributions. In the stratosphere, upward GWMT predominates. The positive upward GWMT associated with the positive intrinsic phase speeds is large in the region where the zonal mean zonal wind is easterly, whereas the negative upward GWMT associated with the negative intrinsic phase speeds is large in the region where the zonal wind is westerly. Positively large upward GWMT associated with the positive intrinsic phase speeds commences suddenly at around day 340 between the tropopause and the zero-wind line at 30 km, whereas negatively large one associated with the negative intrinsic phase speeds commences suddenly at around days 270 and 405 between the tropopause and the zero-wind line at 30 km. After the commencement of the large upward GWMTs, large CMT with the same sign exists around the tropopause for 20–30 days.

In the troposphere, CMT constitutes the most dominant contribution, and downward GWMT constitutes the second most dominant, particularly in the lower troposphere. During an SL-type period from day 315, the CMT associated with the positive intrinsic phase speeds has the same positive sign as that of the negative intrinsic phase speeds, and during another SL-type period from day 375, the CMT associated with the negative intrinsic phase speeds has the same negative sign as that of the positive intrinsic phase speeds. During the BB-type periods, on the other hand, the CMT has opposite sign between the positive and negative intrinsic phase speeds. Hence, the total CMT is large during the SL-type periods whereas it is small during the BB-type periods. The downward GWMT associated with the positive intrinsic phase speeds is large with a negative sign during days 315–375. During this period, the zonal mean zonal wind is westerly in the middle troposphere, where downward-propagating gravity waves are generated. In a similar fashion, the downward GWMT with the negative intrinsic phase speeds is large with a positive sign during days 260–315 and 375–405 when the zonal mean zonal wind is easterly in the middle troposphere.

Figure 14 shows the vertical convergence of the momentum fluxes shown in Fig. 13. In the stratosphere, convergence of the upward GWMT predominates for a limited time interval in the height range around zero-wind lines to produce a large acceleration of the zonal mean zonal wind. In the troposphere, convergence of the CMT comprises the most dominant contribution to the acceleration of the zonal mean zonal wind, and the convergence of the downward GWMT has minor contribution.

7. Discussion

The periodic variations of organized convective systems are obtained in association with the QBO-like oscillation (Figs. 1 and 2). Observational evidence of the QBO modulation of the tropical deep convection has been reported by, for example, Collimore et al. (1998, 2003) and Liess and Geller (2012). Recently, Nie and Sobel (2015) used a cloud-resolving model and showed that tropical deep convection can be modulated by temperature variations in the upper troposphere and lower stratosphere associated with the QBO. Collimore et al. (2003) thought that the QBO modulation of the tropopause height and the vertical shear of the zonal mean zonal wind between the upper troposphere and lower stratosphere may disrupt the coherent structure of

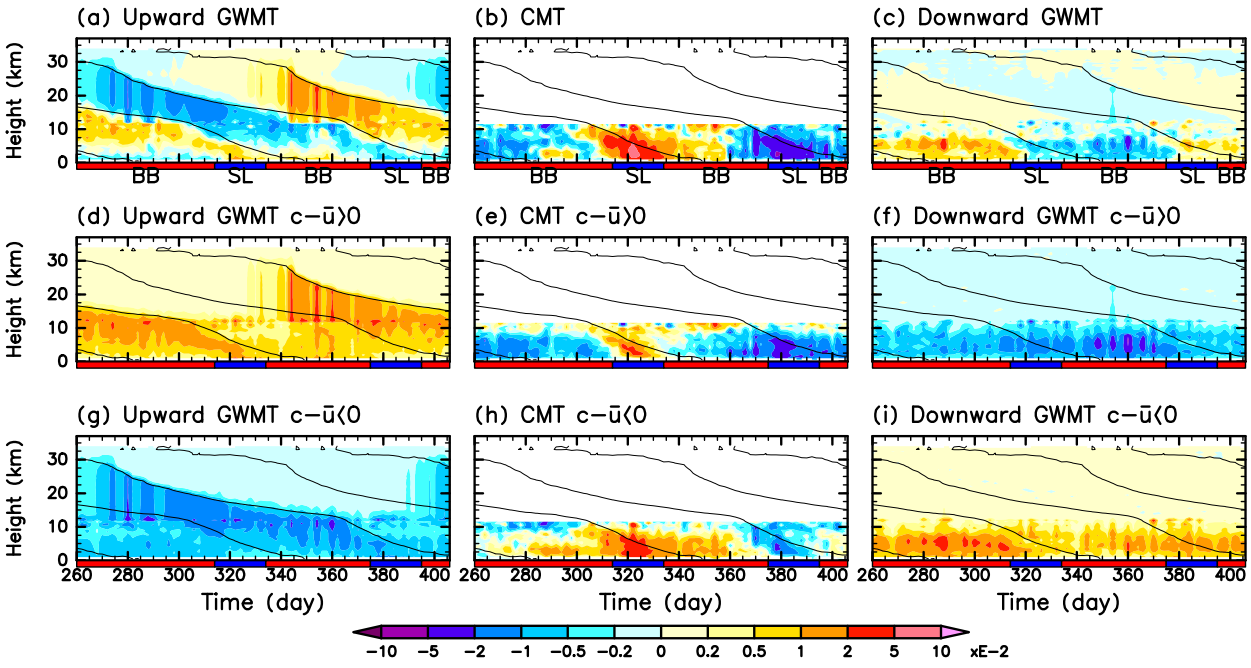

FIG. 13. Time–height sections of momentum transports for (left) upward GWMT, (center) CMT, and (right) downward GWMT. (top) Total value and values integrated over (middle) positive ($c - \bar{u} > 0$) and (bottom) negative ($c - \bar{u} < 0$) intrinsic phase speeds, respectively. The zero-wind lines are overlaid with black contours. Red and blue bars at the bottom of each plot denote BB- and SL-type periods, respectively.

convective plumes and shear off convective clouds. Our QBO-like oscillation is symmetric without the difference between the easterly shear and the westerly shear phases, and thus the convective height and intensity are modulated with a half cycle of the oscillation: Fig. 1c shows that the height of ice clouds is higher and the ice mixing ratio is larger during the SL-type periods than during the BB-type periods. As shown in Fig. 2 (right), the vertical shear of the zonal mean zonal wind between the lower stratosphere and upper troposphere—for example, the wind difference between $z = 12$ and 14 km—is small during the SL-type periods (Figs. 2d,j) compared with during the BB-type periods (Figs. 2b,f,h), consistent with the hypothesis of Collimore et al. on the influence of the mean zonal wind around the tropopause on moist convection.

On the other hand, Liu and Moncrieff (2001) conducted numerical experiments with a two-dimensional cloud-system-resolving model by changing vertical shears of the initial zonal mean zonal wind and showed that the vertical shears in the lower troposphere affects the precipitation patterns and the mesoscale organization of moist convection. In their Fig. 2, the precipitation pattern is of SL type when vertical shear in the lower troposphere is large, whereas it is of BB type when the vertical shear is zero. These are consistent with our results as shown in Fig. 2. Another series of numerical experiments by changing the vertical shear around the tropopause would clarify the relative role of ''bottom up'' and ''top down'' processes in the formation of the SL or BB type of precipitation patterns.

There are three proposed mechanisms of the generation of gravity waves by convection: pure thermal forcing, an ''obstacle'' effect, and a ''mechanical oscillator'' effect [Fritts and Alexander (2003) and references therein]. Alexander et al. (1995) and Piani et al. (2000) showed numerical results that gravity waves generated by a thermal forcing in the absence of strong vertical shear of the zonal mean zonal wind have the vertical wavelengths in the stratosphere that are approximately equal to the vertical extent of the convective heating. In the stratosphere, most of the gravity waves obtained in our model have a vertical wavelength comparable to the vertical extent of the tropospheric moist convection, except for the gravity wave corresponding to A during days 322–323 (Tables 1 and 2). This indicates that the main forcing of those gravity waves in the stratosphere is thermal forcing by latent heat release within the tropospheric moist convection. The gravity wave corresponding to A could be generated by either an obstacle effect or mechanical oscillator effect, and such gravity waves with a short vertical wavelength might have a role to produce the layers of

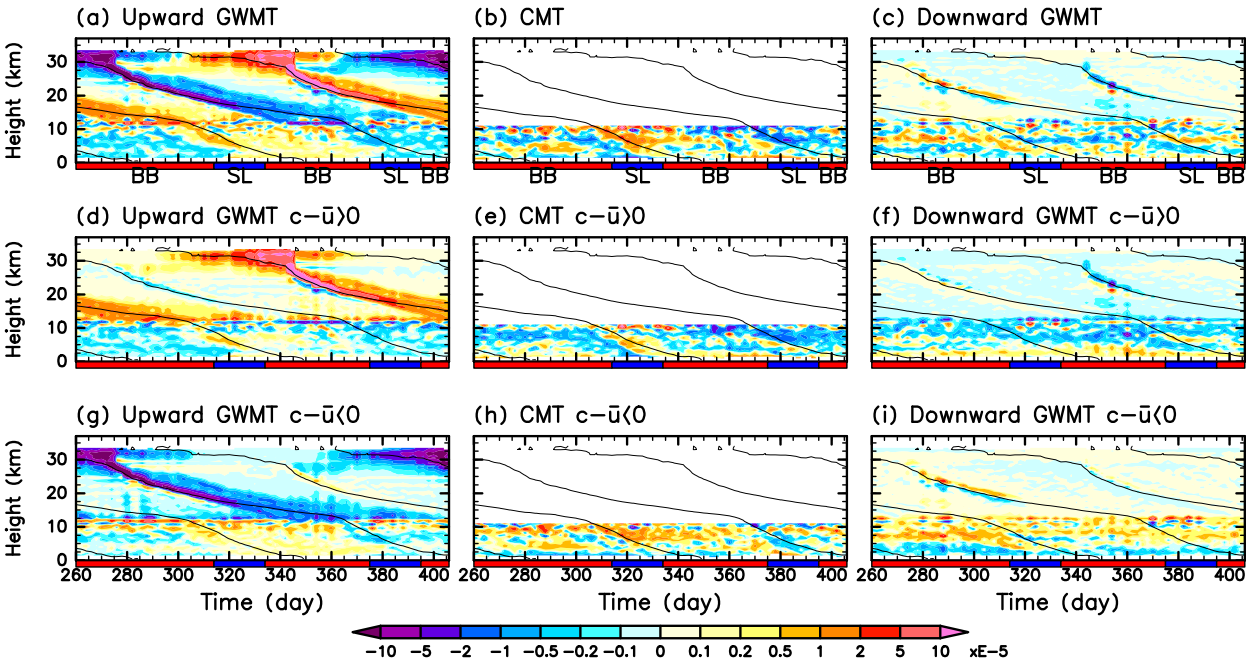

FIG. 14. As in Fig. 13, but for the vertical convergence of momentum flux.

strong convergence and divergence around the tropopause as shown in Fig. 3b.

In the troposphere, the downward-propagating gravity waves obtained in this model have vertical wavelengths of 9–16 km. The upward-propagating gravity waves corresponding to D during days 322–323 and waveform c during days 304–305 appear slightly after the appearance of the downward-propagating gravity waves corresponding to E and d, respectively, in the same region (Figs. 7b,d and 11b,d). They have identical horizontal and vertical wavelengths as those of the corresponding downward-propagating waves (Tables 1 and 2). In addition, waveform D appears below around the altitude of $z = 6$ km (Figs. 8a,c), and waves c and d appear below around $z = 12$ km (Figs. 12a,c); above those levels, there are westerly wind as shown in Figs. 6a and 10a. These results suggest that the downward-propagating waves are reflected at the surface and then propagate upward. Shige (1999) reported the observational evidence of such reflection of gravity waves at the surface whose periods are 1–2 h based on the data from wind profiles during TOGA COARE.

The role of tropospheric gravity waves in the initiation of tropical convection has been studied relying on the idea proposed by Mapes (1993) that tropospheric gravity waves cause the development of new convection through upward displacement at low levels in a mesoscale region surrounding the original convective system. Oouchi (1999) and Shige and Satomura (2001) used two-dimensional cumulus-scale-resolving models to emphasize the role of tropospheric gravity waves generated by a convection system in developing a new convection system. Formation of a new convective system in this model, particularly in the BB-type period, should be related to the gravity waves in the troposphere as described above.

The rapid acceleration just below the Rayleigh damping layer (shown in Fig. 3a) commences suddenly in association with the rapid increase of the vertical flux of horizontal momentum as shown in Fig. 3d and Figs. 13a, 13d, and 13g. In a very simplified and idealized laboratory analog of the QBO (Plumb and McEwan 1978) or its numerical models (Plumb 1977; Yoden and Holton 1988; Wedi and Smolarkiewicz 2006), the switching mechanism of the vertical flux of horizontal momentum can be clearly understood as follows: When the switching of the low-level flow into an easterly (westerly) regime occurs as a result of vertical diffusion near the bottom boundary, the eastward (westward)-propagating wave is no longer attenuated at low levels and penetrates to greater heights to start acceleration of the zonal mean zonal flow (Plumb 1984). In the real atmosphere, on the other hand, the observed oscillation in the zonal mean zonal wind disappears near the tropopause, where the switching mechanism in the idealized system does not work. As Hamilton et al. (2015) stated, this fundamental aspect of the switching mechanism of the QBO in the real atmosphere remains

mysterious. The QBO-like oscillation in our minimal model has a kink in the zonal mean zonal wind near the tropopause with rather different nature of its acceleration in the troposphere (Fig. 1a). Our minimal model of the QBO-like oscillation includes a switching process of the vertical flux of horizontal momentum near the tropopause in a similar way as the real atmosphere without an artificial bottom boundary. It would be a test bed to understand the switching mechanism of the QBO in a simple dynamical framework.

8. Conclusions

Momentum budget of a self-sustained oscillation dynamically analogous to the equatorial QBO obtained in a minimal model of the stratosphere–troposphere coupled system (YBN14) was examined to study the dynamical coupling processes associated with the QBO. The QBO-like oscillation was obtained as a radiative–moist-convective quasi-equilibrium state in a two-dimensional (x–z) cloud-system-resolving nonhydrostatic model with a periodic lateral boundary condition but no effects of the rotation of the earth nor the zonal mean upwelling of the Brewer–Dobson circulation. The obtained QBO-like oscillation shows downward propagation of the zonal mean signals in the stratosphere and associated periodic variations in the troposphere, including cloud properties and precipitation (Fig. 1). The tropospheric variations are characterized by the modulation of organized features of moist-convective systems, with alternating appearance of a squall-line (SL) type and a back-building (BB) type of precipitation patterns (Fig. 2).

An analysis of the momentum budget variation showed that in the stratosphere the acceleration of the zonal mean zonal wind occurs for a limited time interval in a confined layer around zero-wind lines (Fig. 3a). In the troposphere, on the other hand, it occurs rather simultaneously in a wide range of heights. The vertical flux of horizontal momentum (Fig. 3d) and its vertical convergence (Fig. 3b) are large during the BB-type periods in the stratosphere whereas they are large during the SL-type periods in the troposphere.

To examine the vertical momentum transport processes in the troposphere, where gravity waves are generated by convective systems, and in the stratosphere, where waves propagate from the troposphere, we introduced a method that separates the vertical flux of horizontal momentum into three contributions of convective momentum transport (CMT) and momentum transports by upward- and downward-propagating gravity waves (upward and downward GWMTs). First, the phase speed spectra of the upward- and non-upward-propagating contributions for a 2-day interval were estimated using a space–time spectral filter based on the linear theory of gravity waves (Fig. 4, as an example). This part was developed by LM10 and used for the analysis of momentum transports in the troposphere in cloud-system-resolving model simulations by SL13. Then, the CMT spectra, which were estimated from the phase speed spectra of the total cloud (ice plus cloud water) mixing ratio (Figs. 5b and 9b), were subtracted from the spectra of the upward- and non-upward-propagating contributions to obtain the three contributions as given by Figs. 6 and 10. The validity of the method was given by showing that the vertical wind fields related to upward and downward GWMTs satisfy the dispersion relationship of linear gravity waves both for an SL-type period (Table 1 together with Figs. 7 and 8) and for a BB-type period (Table 2 together with Figs. 11 and 12).

Using this method, we quantitatively evaluated the momentum budget through the cycle of the QBO-like oscillation in the minimal model of the stratosphere–troposphere coupled system (Figs. 13 and 14). In the stratosphere, the upward GWMT predominates, and its convergence is the most important factor to accelerate the zonal mean zonal wind. Switching of the zonal mean zonal wind takes place in association with the sudden commencement of large upward GWMTs, which is generated near the tropopause (Figs. 13a,d,g). The generation processes of gravity waves that cause the large upward GWMTs near the tropopause is still unclear and needs further diagnostic studies. The CMT and downward GWMT are confined to the troposphere, and the former is the most dominant contribution to the acceleration of the zonal mean zonal wind. The variations of the mean zonal wind modulate the organization of moist-convective systems with the alternating appearance of SL- and BB-type precipitation patterns. According to the modulation of moist-convective systems, the spectral features of every momentum transport also vary periodically.

The analysis of the stratosphere–troposphere dynamical coupling in this minimal model is a step forward in our understanding of the dynamical coupling processes associated with the equatorial QBO. The method introduced here can be used to quantitatively evaluate the space–time variations of momentum transport processes in the hierarchy of numerical models that include both contributions of convection and gravity waves of upward- and downward-propagating components.

Acknowledgments. The authors thank Marv Geller and two anonymous reviewers for their constructive comments. This work was supported by JSPS KAKENHI (S)

Grant 24224011 and JSPS Core-to-Core Program, B. Asia–Africa Science Platforms.

REFERENCES

Alexander, M. J., and J. R. Holton, 1997: A model study of zonal forcing in the equatorial stratosphere by convectively induced gravity waves. *J. Atmos. Sci.*, **54**, 408–419, doi:10.1175/1520-0469(1997)054<0408:AMSOZF>2.0.CO;2.

——, ——, and D. R. Durran, 1995: The gravity wave response above deep convection in a squall line simulation. *J. Atmos. Sci.*, **52**, 2212–2226, doi:10.1175/1520-0469(1995)052<2212:TGWRAD>2.0.CO;2.

Baldwin, M. P., and Coauthors, 2001: The quasi-biennial oscillation. *Rev. Geophys.*, **39**, 179, doi:10.1029/1999RG000073.

Collimore, C. C., M. H. Hitchman, and D. W. Martin, 1998: Is there a quasi-biennial oscillation in tropical deep convection? *Geophys. Res. Lett.*, **25**, 333–336, doi:10.1029/97GL03722.

——, D. W. Martin, M. H. Hitchman, A. Huesmann, and D. E. Waliser, 2003: On the relationship between the QBO and tropical deep convection. *J. Climate*, **16**, 2552–2568, doi:10.1175/1520-0442(2003)016<2552:OTRBTQ>2.0.CO;2.

Dee, D. P., and Coauthors, 2011: The ERA-Interim reanalysis: Configuration and performance of the data assimilation system. *Quart. J. Roy. Meteor. Soc.*, **137**, 553–597, doi:10.1002/qj.828.

Eliassen, A., and E. Palm, 1961: On the transfer of energy by mountain waves. *Geofys. Publ.*, **22** (3), 94–101.

Fovell, R., D. Durran, and J. R. Holton, 1992: Numerical simulations of convectively generated stratospheric gravity waves. *J. Atmos. Sci.*, **49**, 1427–1442, doi:10.1175/1520-0469(1992)049<1427:NSOCGS>2.0.CO;2.

Fritts, D. C., and M. J. Alexander, 2003: Gravity wave dynamics and effects in the middle atmosphere. *Rev. Geophys.*, **41**, 1003, doi:10.1029/2001RG000106.

Geller, M. A., H. Tanaka, and D. C. Fritts, 1975: Production of turbulence in the vicinity of critical levels for internal gravity waves. *J. Atmos. Sci.*, **32**, 2125–2135, doi:10.1175/1520-0469(1975)032<2125:POTITV>2.0.CO;2.

Hamilton, K., S. Osprey, and N. Butchart, 2015: Modeling the stratosphere's ''heartbeat.'' *Eos, Trans. Amer. Geophys. Union*, **96**, 16–18, doi:10.1029/2015EO032301.

Held, I. M., 2005: The gap between simulation and understanding in climate modeling. *Bull. Amer. Meteor. Soc.*, **86**, 1609–1614, doi:10.1175/BAMS-86-11-1609.

——, R. S. Hemler, and V. Ramaswamy, 1993: Radiative–convective equilibrium with explicit two-dimensional moist convection. *J. Atmos. Sci.*, **50**, 3909–3927, doi:10.1175/1520-0469(1993)050<3909:RCEWET>2.0.CO;2.

Holton, J. R., and R. S. Lindzen, 1972: An updated theory for the quasi-biennial cycle of the tropical stratosphere. *J. Atmos. Sci.*, **29**, 1076–1080, doi:10.1175/1520-0469(1972)029<1076:AUTFTQ>2.0.CO;2.

Horinouchi, T., and S. Yoden, 1998: Wave–mean flow interaction associated with a QBO-like oscillation simulated in a simplified GCM. *J. Atmos. Sci.*, **55**, 502–526, doi:10.1175/1520-0469(1998)055<0502:WMFIAW>2.0.CO;2.

Hoskins, B. J., 1983: Dynamical processes in the atmosphere and the use of models. *Quart. J. Roy. Meteor. Soc.*, **109**, 1–21, doi:10.1002/qj.49710945902.

Lane, T. P., and M. W. Moncrieff, 2010: Characterization of momentum transport associated with organized moist convection and gravity waves. *J. Atmos. Sci.*, **67**, 3208–3225, doi:10.1175/2010JAS3418.1.

Liess, S., and M. A. Geller, 2012: On the relationship between QBO and distribution of tropical deep convection. *J. Geophys. Res.*, **117**, D03108, doi:10.1029/2011JD016317.

Lindzen, R. S., 1990: *Dynamics in Atmospheric Physics: Lecture Notes for an Introductory Graduate-Level Course*. Cambridge University Press, 310 pp.

——, and J. R. Holton, 1968: A theory of the quasi-biennial oscillation. *J. Atmos. Sci.*, **25**, 1095–1107, doi:10.1175/1520-0469(1968)025<1095:ATOTQB>2.0.CO;2.

Liu, C., and M. W. Moncrieff, 2001: Cumulus ensembles in shear: Implications for parameterization. *J. Atmos. Sci.*, **58**, 2832–2842, doi:10.1175/1520-0469(2001)058<2832:CEISIF>2.0.CO;2.

Mapes, B. E., 1993: Gregarious tropical convection. *J. Atmos. Sci.*, **50**, 2026–2037, doi:10.1175/1520-0469(1993)050<2026:GTC>2.0.CO;2.

Moncrieff, M. W., 1992: Organized convective systems: Archetypal dynamical models, mass and momentum flux theory, and parametrization. *Quart. J. Roy. Meteor. Soc.*, **118**, 819–850, doi:10.1002/qj.49711850703.

Nie, J., and A. H. Sobel, 2015: Responses of tropical deep convection to the QBO: Cloud-resolving simulations. *J. Atmos. Sci.*, **72**, 3625–3638, doi:10.1175/JAS-D-15-0035.1.

Oouchi, K., 1999: Hierarchical organization of super cloud cluster caused by WISHE, convectively induced gravity waves and cold pool. *J. Meteor. Soc. Japan*, **77**, 907–927.

Piani, C., D. Durran, M. J. Alexander, and J. R. Holton, 2000: A numerical study of three-dimensional gravity waves triggered by deep tropical convection and their role in the dynamics of the QBO. *J. Atmos. Sci.*, **57**, 3689–3702, doi:10.1175/1520-0469(2000)057<3689:ANSOTD>2.0.CO;2.

Plumb, R. A., 1977: The interaction of two internal waves with the mean flow: Implications for the theory of the quasi-biennial oscillation. *J. Atmos. Sci.*, **34**, 1847–1858, doi:10.1175/1520-0469(1977)034<1847:TIOTIW>2.0.CO;2.

——, 1984: The quasi-biennial oscillation. *Dynamics of the Middle Atmosphere*, J. R. Holton and T. Matsuno, Eds., Terra Scientific Publishing Company, 217–251.

——, and A. D. McEwan, 1978: The instability of a forced standing wave in a viscous stratified fluid: A laboratory analogue of the quasi-biennial oscillation. *J. Atmos. Sci.*, **35**, 1827–1839, doi:10.1175/1520-0469(1978)035<1827:TIOAFS>2.0.CO;2.

Shaw, T. A., and T. P. Lane, 2013: Toward an understanding of vertical momentum transports in cloud-system-resolving model simulations of multiscale tropical convection. *J. Atmos. Sci.*, **70**, 3231–3247, doi:10.1175/JAS-D-13-068.1.

Shige, S., 1999: Disturbances of 1–2 hour-periods observed in the tropical lower troposphere during the TOGA-COARE IOP. *J. Meteor. Soc. Japan*, **77**, 1123–1136.

——, and T. Satomura, 2001: Westward generation of eastward-moving tropical convective bands in TOGA COARE. *J. Atmos. Sci.*, **58**, 3724–3740, doi:10.1175/1520-0469(2001)058<3724:WGOEMT>2.0.CO;2.

Skamarock, W. C., and Coauthors, 2008: A description of the Advanced Research WRF version 3. NCAR Tech. Note NCAR/TN-475+STR, 113 pp., doi:10.5065/D68S4MVH.

Takahashi, M., 1993: A QBO-like oscillation in a two-dimensional model derived from a GCM. *J. Meteor. Soc. Japan*, **71**, 641–654.

Watanabe, S., and Y. Kawatani, 2012: Sensitivity of the QBO to mean tropical upwelling under a changing climate simulated with an earth system model. *J. Meteor. Soc. Japan*, **90A**, 351–360, doi:10.2151/jmsj.2012-A20.

Wedi, N. P., and P. K. Smolarkiewicz, 2006: Direct numerical simulation of the Plumb–McEwan laboratory analog of the QBO. *J. Atmos. Sci.*, **63**, 3226–3252, doi:10.1175/JAS3815.1.

Yoden, S., and J. R. Holton, 1988: A new look at equatorial quasi-biennial oscillation models. *J. Atmos. Sci.*, **45**, 2703–2717, doi:10.1175/1520-0469(1988)045<2703:ANLAEQ>2.0.CO;2.

——, H.-H. Bui, and E. Nishimoto, 2014: A minimal model of QBO-like oscillation in a stratosphere–troposphere coupled system under a radiative–moist convective quasi-equilibrium state. *SOLA*, **10**, 112–116, doi:10.2151/sola.2014-023.